Dark solitons in the Lugiato-Lefever equation with normal dispersion

P. Parra-Rivas,[1,2] E. Knobloch,[3] D. Gomila,[2] and L. Gelens[1,4,5]

[1]*Applied Physics Research Group, APHY, Vrije Universiteit Brussel, 1050 Brussels, Belgium*

[2]*Instituto de Física Interdisciplinar y Sistemas Complejos, IFISC (CSIC-UIB), Campus Universitat de les Illes Balears, E-07122 Palma de Mallorca, Spain*

[3]*Department of Physics, University of California, Berkeley, California 94720, USA*

[4]*Department of Chemical and Systems Biology, Stanford University School of Medicine, Stanford, California 94305, USA*

[5]*Laboratory of Dynamics in Biological Systems, KU Leuven Department of Cellular and Molecular Medicine, University of Leuven, B-3000 Leuven, Belgium*

(Received 10 March 2016; published 22 June 2016)

The regions of existence and stability of dark solitons in the Lugiato-Lefever model with normal chromatic dispersion are described. These localized states are shown to be organized in a bifurcation structure known as collapsed snaking implying the presence of a region in parameter space with a finite multiplicity of dark solitons. For some parameter values dynamical instabilities are responsible for the appearance of oscillations and temporal chaos. The importance of the results for understanding frequency comb generation in microresonators is emphasized.

DOI: 10.1103/PhysRevA.93.063839

I. INTRODUCTION

Dark solitons, localized spots of lower intensity embedded in a homogeneous surrounding, are a particular type of soliton appearing in conservative or dissipative systems far from thermodynamic equilibrium [1]. In the latter case they are known as dissipative solitons (DSs) and related structures can be found in a large variety of systems, including those found in chemistry [2], gas discharges [3], fluid mechanics [4], vegetation and plant ecology [5], as well as optics [6], where they are known as cavity solitons. These structures arise as a result of a balance between nonlinearity and spatial coupling, and between driving and dissipation. In this work we focus on the field of optics, and study DSs in single mode fiber resonators and microresonators where they are known as temporal solitons [7]. These systems are commonly described by the Lugiato-Lefever equation (LLE), a mean-field model originaly introduced in [8] in the context of ring cavities or a Fabry-Perot interferometer with transverse spatial extent, partially filled with a nonlinear medium. In temporal systems bright and dark solitons can be found. Taking into account only second-order dispersion (SOD) two regimes can be identified, characterized by either normal or anomalous chromatic dispersion. In the latter case the only type of DSs that exist are bright solitons arising in both the monostable [9] and bistable regimes [10–12]. In contrast, in the normal SOD case the main type of DSs that appear are dark solitons [12–15]. In this work we provide a detailed analysis of the bifurcation structure and stability of dark DSs appearing in the normal dispersion regime, classifying the different dynamical regimes arising in this system.

The organization of this paper is as follows. In Sec. II, we introduce the Lugiato-Lefever model in the context of temporal dynamics in fiber resonators and microresonators. We then analyze the spatial stability properties of spatially uniform states (Sec. III), followed in Sec. IV by an analysis of the bifurcation structure of dark solitons. In Sec. V we analyze oscillatory and chaotic dynamics of dark solitons. In Sec. VI we summarize the main results of the analysis presented in the earlier sections and conclude in Sec. VII by discussing their implications for frequency comb generation in nonlinear optics.

II. LUGIATO-LEFEVER EQUATION

In this section we provide a brief introduction to the LLE in the context of fiber resonators and microresonators. We then employ the normalization of [10] to study the continuous-wave (cw) or equivalently the homogeneous steady state (HSS) solutions of this model and determine their temporal stability properties. Figure 1 shows a fiber cavity of length L with a beam splitter with transmission coefficient T and a continuous-wave source of amplitude E_0. At the beam splitter, the pump is coupled to the electromagnetic wave circulating inside the fiber. Under these conditions the evolution of the electric field $E \equiv E(t',\tau)$ within the cavity is described by the following evolution equation [16]:

$$t_R \frac{\partial E}{\partial t'} = -(\alpha + i\delta_0)E - i\frac{L\beta_2}{2}\frac{\partial^2 E}{\partial \tau^2} + i\gamma L|E|^2 E + \sqrt{T}E_0, \tag{1}$$

where $\alpha > 0$ describes the total cavity losses, β_2 is the second-order dispersion coefficient ($\beta_2 > 0$ in the normal dispersion case while $\beta_2 < 0$ in the anomalous case), $\gamma > 0$ is a nonlinear coefficient arising from the Kerr effect in the resonator, and δ_0 is the cavity detuning. Here τ is the fast time describing the temporal structure of the nonlinear waves while the slow time t' corresponds to the evolution time scale over many round trips, each of duration t_R. After normalizing Eq. (1) we arrive at the dimensionless mean-field LLE [8]:

$$\partial_t A = -(1 + i\theta)A + i\nu\partial_x^2 A + i|A|^2 A + \rho, \tag{2}$$

where $A(x,t) \equiv E(t',\tau)\sqrt{\gamma L/\alpha}$ is a complex scalar field, $t \equiv \alpha t'/t_R$, $x \equiv \tau\sqrt{2\alpha/(L|\beta_2|)}$, $\rho = E_0\sqrt{\gamma L T/\alpha^3}$, and $\theta = \delta_0/\alpha$. In the following we refer to the variable x as a spatial coordinate by analogy with other resonantly driven systems

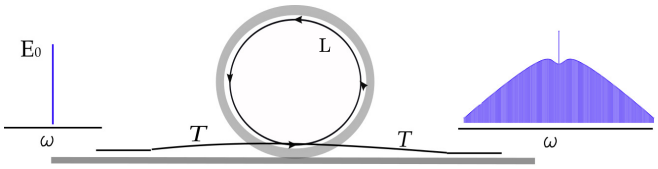

FIG. 1. A synchronously pumped fiber cavity. Here T is the transmission coefficient of the beam splitter and L is the length of the fiber.

such as the LLE for spatially extended optical cavities [6,8] or the parametrically forced Ginzburg-Landau equation [17].

Owing to the periodic nature of fiber cavities and microresonators, we consider periodic boundary conditions, i.e., $A(0,t) = A(L,t)$, where L is now the dimensionless length of the system and choose $L = 160$ for all numerical computations. The parameters $\rho,\theta \in \mathbb{R}$ correspond to the normalized injection and detuning, respectively, and serve as the control parameters of this system. The parameter ν represents the SOD coefficient and is also normalized: $\nu = -1$ in the normal dispersion case and $\nu = 1$ in the anomalous dispersion case [9–12]. The present work is restricted to the case $\nu = -1$.

The steady states of Eq. (2) are solutions of the ordinary differential equation (ODE)

$$i\nu\frac{d^2A}{dx^2} - (1+i\theta)A + i|A|^2A + \rho = 0 \tag{3}$$

and are either spatially uniform states (HSSs) or spatially nonuniform states, consisting either of a periodic pattern (a spatially periodic state PS) or spatially localized states (DSs). In this section we focus on the HSSs, $A \equiv A_0$, leaving for subsequent sections the study of the other states. The A_0 states solve the classic cubic equation of dispersive optical bistability, namely

$$I_0^3 - 2\theta I_0^2 + (1+\theta^2)I_0 = \rho^2, \tag{4}$$

where $I_0 \equiv |A_0|^2$. For $\theta < \sqrt{3}$, Eq. (4) is single valued and hence the system is monostable [see Fig. 2(a)]. For $\theta > \sqrt{3}$, Eq. (4) is triple valued as shown in Figs. 2(b)–2(d). The transition between the three different solutions occurs via the two saddle nodes $\mathrm{SN}_{\mathrm{hom},1}$ and $\mathrm{SN}_{\mathrm{hom},2}$ located at

$$I_\pm \equiv |A_\pm|^2 = \frac{2\theta}{3} \pm \frac{1}{3}\sqrt{\theta^2 - 3}. \tag{5}$$

In the following we will denote the bottom solution branch (from $I_0 = 0$ to I_-) by A_0^b, the middle branch between I_- and I_+ by A_0^m, and the top branch by A_0^t ($I_0 > I_+$). In terms of the real, $U \equiv \mathrm{Re}[A]$, and imaginary, $V \equiv \mathrm{Im}[A]$, parts the HSSs $A = A_0$ take the form

$$\begin{bmatrix} U_0 \\ V_0 \end{bmatrix} = \begin{bmatrix} \frac{\rho}{1+(I_0-\theta)^2} \\ \frac{(I_0-\theta)\rho}{1+(I_0-\theta)^2} \end{bmatrix}. \tag{6}$$

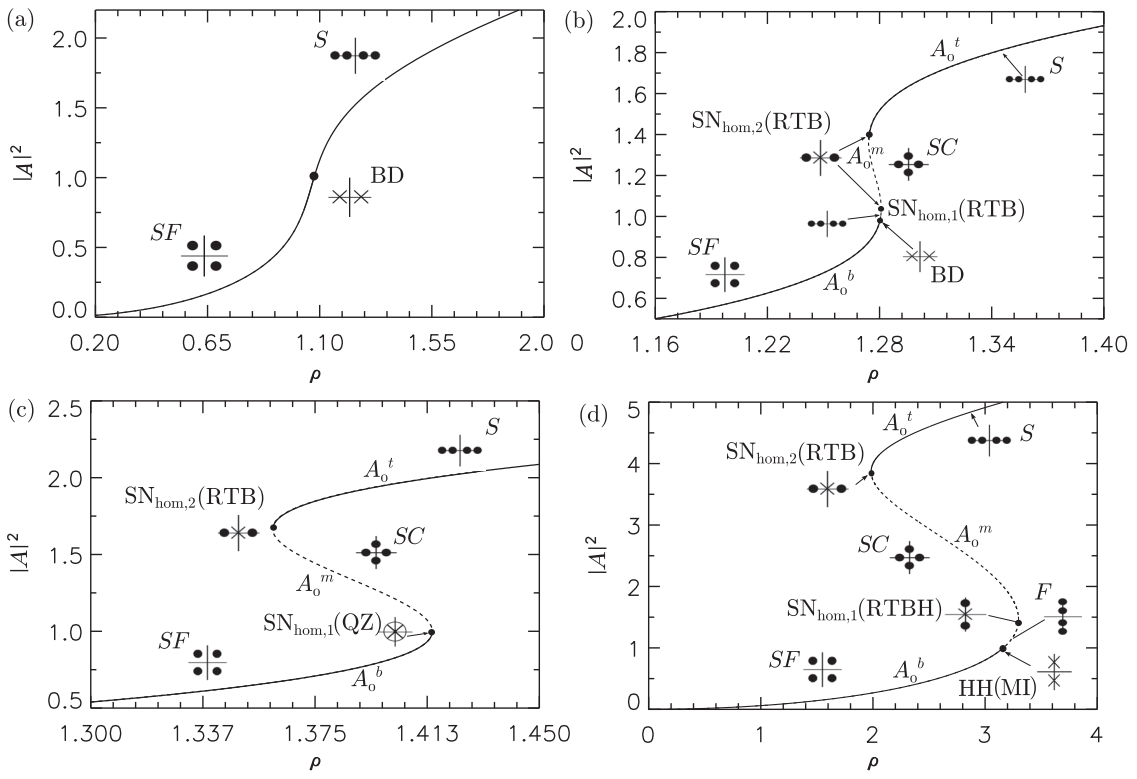

FIG. 2. Spatial eigenvalues of A_0 for several values of θ. (a) $\theta = 1.4 < \sqrt{3}$; (b) $\sqrt{3} < \theta = 1.8 < 2$; (c) $\theta = 2$; (d) $2 < \theta = 4$. Solid (dashed) lines indicate stability (instability) in time. SF: saddle focus; S: saddle; F: center; SC: saddle center; RTB: reversible Takens-Bogdanov; RTBH: reversible Takens-Bogdanov-Hopf; BD: Belyakov-Devaney; HH(MI): Hamiltonian-Hopf; QZ: quadruple zero. A list of these transitions in the spatial eigenspectrum and their codimension is given in Table I.

We next analyze the linear stability of the HSSs to perturbations of the form

$$\begin{bmatrix} U \\ V \end{bmatrix} = \begin{bmatrix} U_0 \\ V_0 \end{bmatrix} + \epsilon \begin{bmatrix} a \\ b \end{bmatrix} e^{ikx+\Omega t} + \text{c.c.}, \tag{7}$$

where k represents the wave number of the perturbation. We find that the growth rate $\Omega(k)$ is given by

$$\Omega(k) = -1 \pm \sqrt{4I_0\theta - 3I_0^2 - \theta^2 + (4I_0 - 2\theta)\nu k^2 - k^4}. \tag{8}$$

It follows that in the monostable regime the A_0 solution is always stable while for $\sqrt{3} < \theta < 2$ the A_0^b and A_0^t states are stable and A_0^m is unstable. These results are reflected in the diagrams shown in Figs. 2(a) and 2(b). However, when $\theta > 2$ the A_0^b branch becomes unstable at a steady-state bifurcation with $k \neq 0$. This Turing or modulational instability (MI) occurs at $I_0 = 1$ and generates a stationary periodic wave train with wave number $k_0 = \sqrt{\nu(2-\theta)}$; A_0^m remains unstable while A_0^t is always stable. From a spatial dynamics point of view (Sec. III) the MI bifurcation corresponds to a Hamiltonian-Hopf bifurcation in space (HH). No Hopf bifurcations in time of the HSSs are possible.

III. SPATIAL DYNAMICS

In this section we investigate the conditions that are necessary for the presence of exponentially localized states that approach A_0 as $x \to \pm\infty$. To obtain these conditions we first rewrite Eq. (3) as a dynamical system,

$$\begin{aligned} \frac{dU}{dx} &= \tilde{U}, \quad \frac{dV}{dx} = \tilde{V}, \\ \frac{d\tilde{U}}{dx} &= \nu[V + \theta U - UV^2 - U^3], \\ \frac{d\tilde{V}}{dx} &= \nu[-U + \theta V - VU^2 - V^3 + \rho], \end{aligned} \tag{9}$$

and employ the approach of spatial dynamics, i.e., we think of the solutions of Eq. (9) as evolving in x, the rescaled fast time, from $x = -\infty$ to $x = \infty$ [9,17–20]. Thus DSs correspond to *homoclinic orbits* of Eq. (9). This term is used to refer to orbits (trajectories) connecting a fixed point (equilibrium) to itself. In the spatial dynamical context a fixed point corresponds to a homogeneous state: $dU/dx = dV/dx = d\tilde{U}/dx = d\tilde{V}/dx = 0$. We shall also be interested in heteroclinic orbits, i.e., trajectories connecting a fixed point a to a different fixed point b. Such orbits represent (stationary) fronts connecting two different homogeneous states. We employ the terminology heteroclinic *cycle* to refer to a pair of orbits, one connecting a to b and the other b to a. A heteroclinic cycle thus corresponds to a pair of back-to-back fronts.

The fixed points of Eq. (9) are the HSSs A_0 of the original evolution equation (2). The stability of these fixed points (in space) is determined by the eigenspectrum of the Jacobian of the system (9) around $A_0 \equiv U_0 + iV_0$, namely

$$\mathcal{J} = \nu \begin{bmatrix} 0 & 0 & \nu & 0 \\ 0 & 0 & 0 & \nu \\ \theta - V^2 - 3U^2 & 1 - 2UV & 0 & 0 \\ -(1 + 2UV) & \theta - U^2 - 3V^2 & 0 & 0 \end{bmatrix}_{(U_0, V_0)}. \tag{10}$$

The four eigenvalues of $\mathcal{J}$ satisfy the biquadratic equation

$$\lambda^4 + (4I_0 - 2\theta)\nu\lambda^2 + \theta^2 + 3I_0^2 - 4\theta I_0 + 1 = 0. \tag{11}$$

The form of this equation is a consequence of spatial reversibility [21–23], i.e., the invariance of Eq. (2) under the transformation $(x, A) \mapsto (-x, A)$, or equivalently the invariance of the system (9) under $(x, U, V, \tilde{U}, \tilde{V}) \mapsto (-x, U, V, -\tilde{U}, -\tilde{V})$. This invariance implies that if λ is a spatial eigenvalue, so are $-\lambda$ and $\pm\lambda^*$, where * indicates complex conjugation. Consequently there are four possibilities:

(1) the eigenvalues are real: $\lambda_{1,2,3,4} = (\pm q_1, \pm q_2)$;

(2) there is a quartet of complex eigenvalues: $\lambda_{1,2,3,4} = (\pm q_0 \pm ik_0)$;

(3) the eigenvalues are imaginary: $\lambda_{1,2,3,4} = (\pm ik_1, \pm ik_2)$;

(4) two eigenvalues are real and two imaginary: $\lambda_{1,2,3,4} = (\pm q_0, \pm ik_0)$.

A sketch of these possible eigenvalue configurations is shown in Fig. 3, and their names and codimension are provided in Table I. The transition from case 1 to case 2 is through a Belyakov-Devaney (BD) [18,19] point with eigenvalues $(\pm q_0, \pm q_0)$, while the transition from case 2 to case 3 is via a Hamiltonian-Hopf (HH) bifurcation [18,24], with $\lambda_{1,2,3,4} = (\pm ik_0, \pm ik_0)$. The transition from case 1 to case 4 is via a reversible Takens-Bogdanov (RTB) bifurcation with eigenvalues $\lambda_{1,2,3,4} = (\pm q_0, 0, 0)$ [18,19] while the transition from case 3 to case 4 is via a reversible Takens-Bogdanov-Hopf (RTBH) bifurcation with eigenvalues $\lambda_{1,2,3,4} = (\pm ik_0, 0, 0)$ [18,19]. The unfolding of all these scenarios is related to the quadruple zero (QZ) codimension-2 point [18,19]. As shown in the next section the transitions between these different regimes organize the parameter space for DSs.

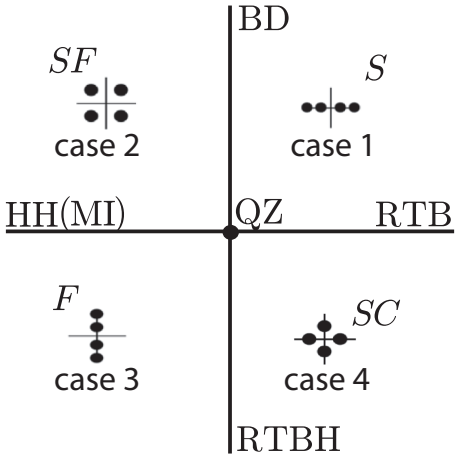

FIG. 3. Sketch of the possible organization of spatial eigenvalues λ satisfying the biquadratic equation (11) for a spatially reversible system. The acronyms corresponding to the different labels are as in Fig. 2.

TABLE I. Nomenclature used to refer to different transitions in the spatial eigenspectrum, labeled in Fig. 3.

Cod	$(\lambda_{1,2,3,4})$	Name
Zero	$(\pm q_0 \pm ik_0)$	saddle focus
Zero	$(\pm q_1, \pm q_2)$	saddle
Zero	$(\pm ik_1, \pm ik_2)$	center
Zero	$(\pm q_0, \pm ik_0)$	saddle center
One	$(\pm q_0, 0, 0)$	reversible Takens-Bogdanov
One	$(\pm ik_0, 0, 0)$	reversible Takens-Bogdanov-Hopf
One	$(\pm q_0, \pm q_0)$	Belyakov-Devaney
One	$(\pm ik_0, \pm ik_0)$	Hamiltonian-Hopf
Two	$(0,0,0,0)$	quadruple zero

The eigenvalues satisfying Eq. (11) are

$$\lambda = \pm\sqrt{(\theta - 2I_0)\nu \pm \sqrt{I_0^2 - 1}}. \tag{12}$$

Figure 2 summarizes the possible eigenvalue configurations for normal dispersion ($\nu = -1$). The transition at $I_0 = 1$, i.e., along the green curve

$$\rho = \sqrt{1 + (1-\theta)^2} \tag{13}$$

in Fig. 4, corresponds to a BD transition when $\theta < 2$ and an HH transition when $\theta > 2$. Figures 2(a) and 2(b) correspond to the case $\theta < 2$; we see that the saddle-node bifurcation at $\mathrm{SN}_{\mathrm{hom},1}$ corresponds to a RTB bifurcation. In contrast, for $\theta > 2$ $\mathrm{SN}_{\mathrm{hom},1}$ has become a RTBH bifurcation [Fig. 2(d)]. For $\theta = 2$ [Fig. 2(c)] the BD, HH, RTB, and RTBH lines meet at the QZ point. In the parameter space of Fig. 4 the QZ point corresponds to $(\theta, \rho) = (2, \sqrt{2})$. The other relevant bifurcation lines in this scenario correspond to $\mathrm{SN}_{\mathrm{hom},2}$. This point corresponds to a RTB bifurcation in space regardless of the value of θ.

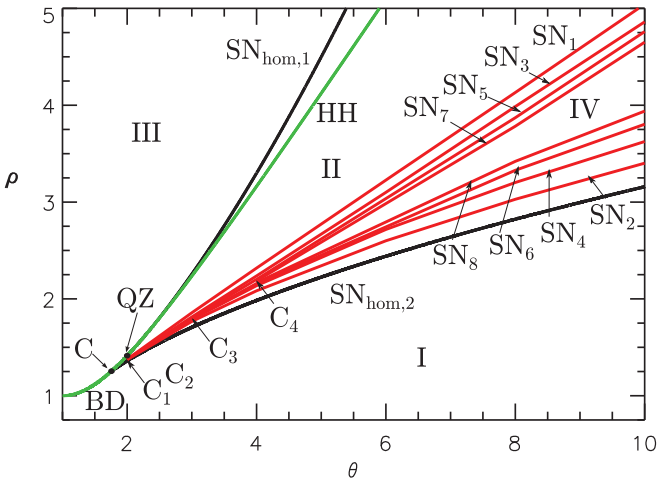

FIG. 4. The (θ, ρ) parameter space for normal dispersion in the region of existence of dark solitons. The green line corresponds to the HH bifurcation, the black lines to SN bifurcations of the HSS, and the red lines to SN bifurcations of the dark DSs. The bifurcation lines and the regions I–IV are discussed in more detail in the text.

In terms of spatial dynamics, DSs correspond to intersections of the stable and unstable manifolds of the HSS [23]. In cases 1 and 2 the HSS has a two-dimensional stable and a two-dimensional unstable manifold. These manifolds are transverse to the two-dimensional fixed point subspace of the symmetry $(x, A) \mapsto (-x, A)$ and hence intersect in a structurally stable way. Therefore we expect DSs in cases 1 and 2 only. In case 4, the stable and unstable manifolds of the HSS are one dimensional and DSs, although possible, are exceptional [25]. In Fig. 2(b) DSs bifurcate from both $\mathrm{SN}_{\mathrm{hom},1}$ and $\mathrm{SN}_{\mathrm{hom},2}$. When HH is present [Fig. 2(d)] DSs bifurcate from HH and from $\mathrm{SN}_{\mathrm{hom},2}$.

In Sec. IV A we show that it is possible to compute DSs analytically near the bifurcation points that produce them, and use the resulting expressions to initialize numerical continuation [26] of these states.

IV. BIFURCATIONS AND EXISTENCE OF DISSIPATIVE SOLITONS

A. Weakly nonlinear analysis

In this section we compute weakly nonlinear DSs using multiple scale perturbation theory near the RTB bifurcation corresponding to $\mathrm{SN}_{\mathrm{hom},2}$. The procedure applies equally around the other RTB point at $\mathrm{SN}_{\mathrm{hom},1}$. Following [17], we fix the value of θ and suppose that the DSs at $\rho \approx \rho_t$, where $\rho = \rho_t$ corresponds to the $\mathrm{SN}_{\mathrm{hom},2}$ bifurcation, are captured by the ansatz $U = U^* + u$, $V = V^* + v$, where U^* and V^* represent the HSS A_0^t and u and v capture the spatial dependence. We next introduce appropriate asymptotic expansions for each variable in terms of a small parameter ϵ defined through the relation $\rho = \rho_t + \epsilon^2\delta$, where δ is defined in the Appendix. Each variable is written in the form

$$\begin{bmatrix} U^* \\ V^* \end{bmatrix} = \begin{bmatrix} U_t \\ V_t \end{bmatrix} + \epsilon \begin{bmatrix} U_1 \\ V_1 \end{bmatrix} + \cdots \tag{14}$$

and

$$\begin{bmatrix} u \\ v \end{bmatrix} = \epsilon \begin{bmatrix} u_1 \\ v_1 \end{bmatrix} + \epsilon^2 \begin{bmatrix} u_2 \\ v_2 \end{bmatrix} + \cdots \tag{15}$$

and these expressions are inserted into Eq. (3). Solving order by order in ϵ we find that the leading-order asymptotic solution close to the RTB point is given by

$$\begin{bmatrix} U \\ V \end{bmatrix} = \begin{bmatrix} U_t \\ V_t \end{bmatrix} + \epsilon \begin{bmatrix} U_1 + u_1 \\ V_1 + v_1 \end{bmatrix}, \tag{16}$$

where U_t and V_t correspond to the HSS at $\rho = \rho_t$, and

$$\begin{bmatrix} u_1 \\ v_1 \end{bmatrix} = \begin{bmatrix} U_1 \\ V_1 \end{bmatrix} \psi(x), \tag{17}$$

with

$$\begin{bmatrix} U_1 \\ V_1 \end{bmatrix} = \mu \begin{bmatrix} 1 \\ \eta \end{bmatrix} \tag{18}$$

and

$$\psi(x) = -3\mathrm{sech}^2\left[\frac{1}{2}\sqrt{-\frac{\alpha_2}{\alpha_1}}\left(\frac{\rho - \rho_t}{\delta}\right)^{1/4} x\right]. \tag{19}$$

Here η, μ, α_1, and α_2 are parameters defined in the Appendix, where the details of the calculation can be found.

The localized structure defined by the asymptotic solution is shown in Fig. 22 of the Appendix; the negative sign in Eq. (19) implies that the solution is a hole in the background A_0^t state, i.e., a dark soliton. Of course, on a large domain we expect to find states with two or more dark solitons as well. When these are well separated these states behave like one-soliton states and so should bifurcate from the vicinity of $SN_{hom,2}$ just like the one-soliton states.

We now discuss the bifurcation structure of dark solitons in two regimes: the bistable region before the QZ point, namely for $\sqrt{3} < \theta < 2$, and the bistable region after QZ, i.e., for $\theta > 2$, and use this bifurcation structure to explain how the Maxwell point (defined below) mediates between dark solitons and states we refer to as bright solitons. The dark solitons represent states with intensity below the background intensity $|A_0^t|^2$ while the bright solitons represent states with intensity that exceeds the lower background intensity $|A_0^b|^2$ (Fig. 2). The latter could therefore also be referred to as antidark solitons [27].

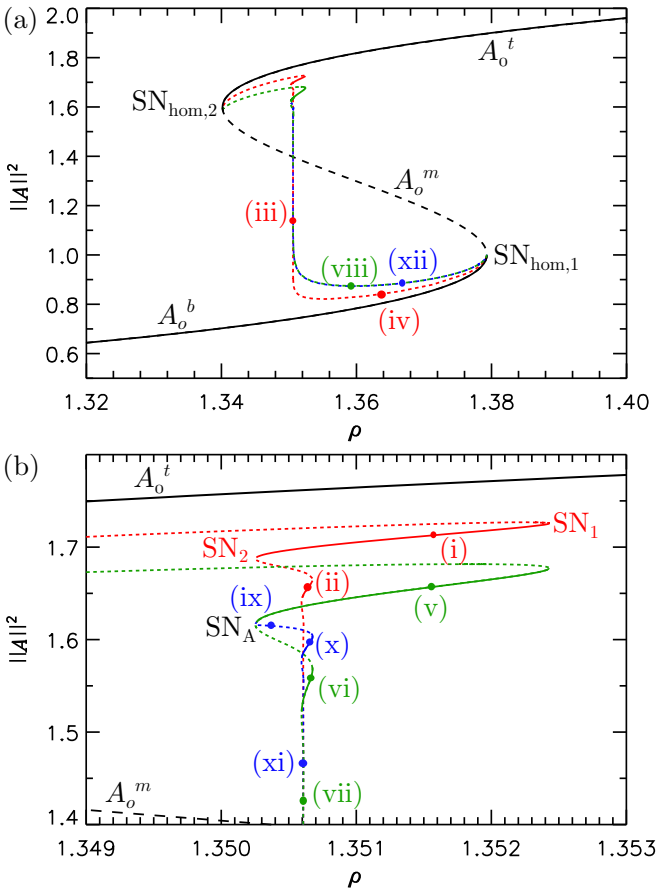

FIG. 5. (a) Bifurcation diagram at $\theta = 1.95$. (b) Zoom of panel (a) around $SN_{hom,2}$. The homogeneous steady states HSS are shown in black, one-soliton states in red and two-soliton states in green. A branch of nonidentical two-soliton states bifurcates from the branch of identical two-soliton states near SN_A and is shown in blue. All undergo collapsed snaking in the vicinity of $\rho_M \approx 1.350\,607\,4$. Temporally stable (unstable) DSs are indicated using solid (dashed) lines. Profiles corresponding to the labeled locations are shown in Fig. 6 and in more detail in Fig. 7.

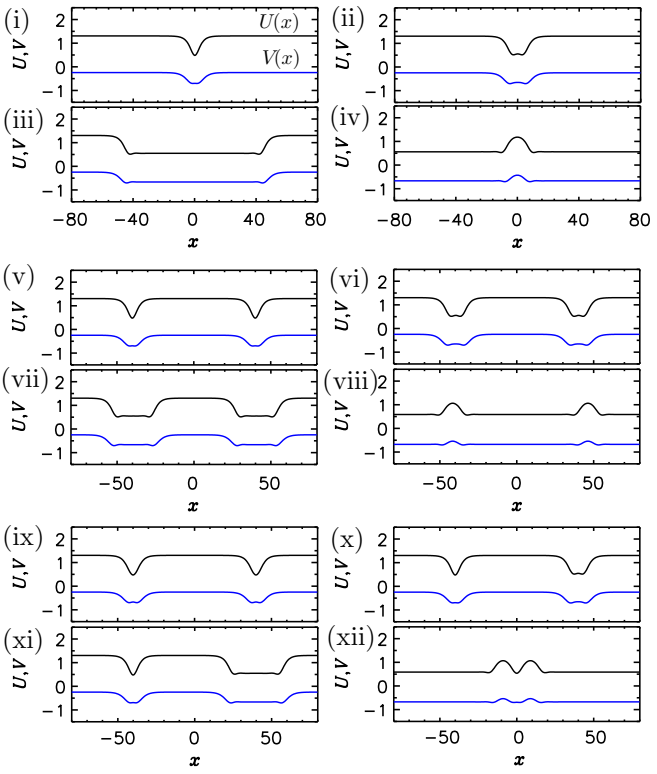

FIG. 6. Spatial profiles of DSs (dark and bright one-soliton and two-soliton states) corresponding to the locations indicated in Figs. 5(a) and 5(b), with $U(x)$ in black and $V(x)$ in blue. Near $SN_{hom,2}$ the states resemble holes (dark solitons) while near $SN_{hom,1}$ they resemble localized pulses (bright solitons).

B. Dark solitons for $\sqrt{3} < \theta < 2$

In the following we use the L^2 norm, $||A||^2 \equiv \frac{1}{L}\int_0^L |A|^2\,dx$, to represent the DSs in a bifurcation diagram. Figure 5, computed for $\theta = 1.95$, reveals the presence of a branch of single dark solitons in the domain (hereafter the one-soliton state, red curve). This branch bifurcates from HSS very close to $SN_{hom,2}$, as anticipated in the preceding section, and undergoes collapsed snaking [28–30], i.e., it undergoes a series of exponentially decaying oscillations in the vicinity of a critical value of ρ, hereafter $\rho = \rho_M \approx 1.350\,607\,4$. During this process the hole corresponding to the dark soliton deepens, forming a pair of fronts connecting A_0^t and A_0^b and then broadens as the A_0^b state expels A_0^t [Fig. 6, profiles (i)–(iii)], becoming in an infinite system a heteroclinic cycle between A_0^t and A_0^b at ρ_M. In gradient systems this point corresponds to the so-called Maxwell point, where both homogeneous solutions have equal energy. In nongradient systems, such as LLE, such a cycle may still be present, even though an energy cannot be defined, and we retain this terminology to refer to its location, i.e., the parameter value corresponding to the presence of a pair of stationary, infinitely separated fronts connecting A_0^t to A_0^b and back again. The successive saddle nodes seen in Fig. 5 correspond to the appearance of additional oscillations in the tails of the fronts as the local maximum (minimum) at the symmetry point $x = 0$ turns into a local minimum (maximum) and back again, and hence to a gradual increase in the width of the hole. Figure 7 shows a detail of this process. The associated

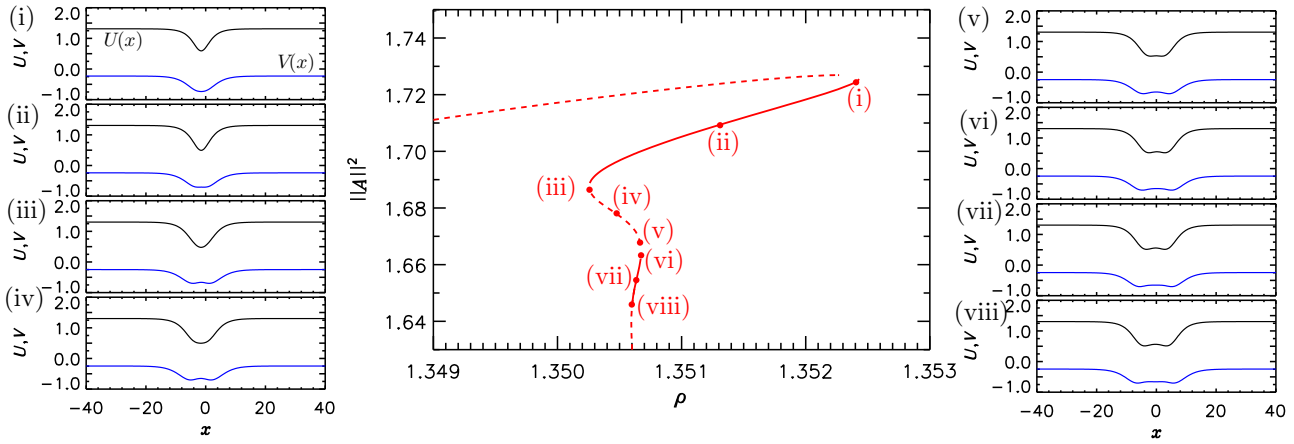

FIG. 7. Spatial profiles of dark solitons near the upper end of the $\theta = 1.95$ one-soliton branch at locations indicated in the middle panel, showing that the splitting of the central peak (dip) in $(U(x), V(x))$, shown in black and red, respectively, occurs at different locations along the branch.

hole states are temporally stable between SN_1 and SN_2, and on all the subsequent branch segments with positive slope [28,29], shown using solid lines. A profile of a stable localized hole on the SN_1-SN_2 segment is shown in Fig. 6(i). For the value of θ used in Fig. 5 the collapse of the saddle nodes to ρ_M is very abrupt because the spatial oscillations in the tail of the front decay very fast. Figure 8 shows a clearer example of the behavior in this region, albeit for a larger value of θ.

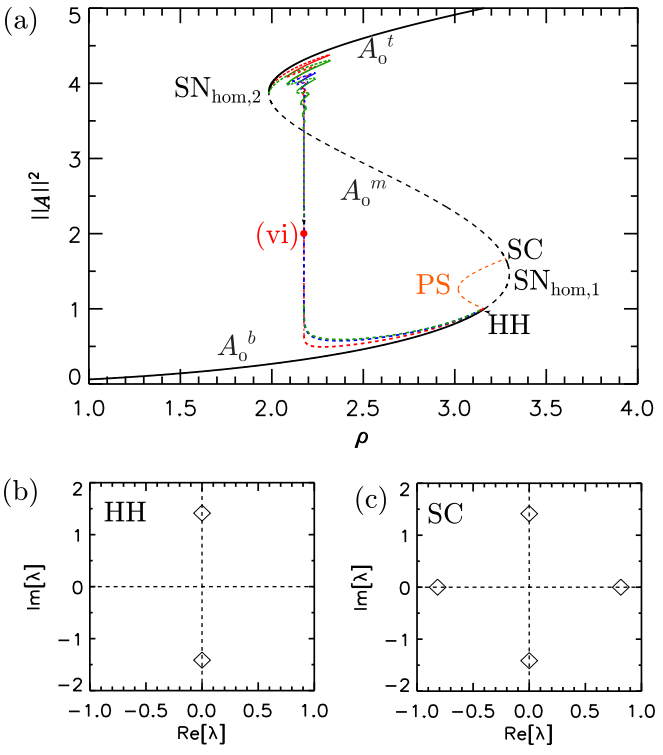

FIG. 8. (a) Bifurcation diagram for $\theta = 4$ showing collapsed defect-mediated snaking of one-soliton (red line) and two-soliton (green line) branches, showing their reconnection with the PS branch (orange line) that bifurcates from HH on A_0^b. Temporally stable (unstable) structures are indicated using solid (dashed) lines. Black lines correspond to HSS. Enlargements of panel (a) can be found in Figs. 9 and 12. (b) The spatial eigenvalues λ of A_0 at locations HH and SC in (a).

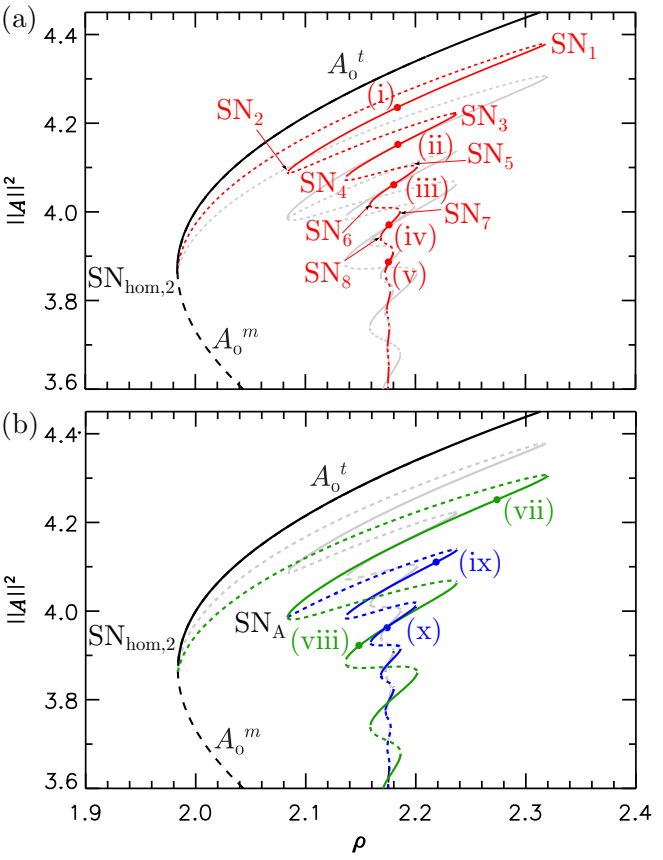

FIG. 9. Detail of the one-soliton [panel (a), red line] and two-soliton [panel (b), green line] branches in the vicinity of $SN_{hom,2}$ for $\theta = 4$. Black lines show the homogeneous states HSS. Panel (b) also shows a family of nonidentical two-soliton states (blue line) that bifurcate from the saddle node SN_A on the two-soliton branch and also undergo collapsed defect-mediated snaking. Temporally stable (unstable) structures are indicated using solid (dashed) lines. Profiles corresponding to the labeled locations are shown in Fig. 10, with details of this process shown in Fig. 11.

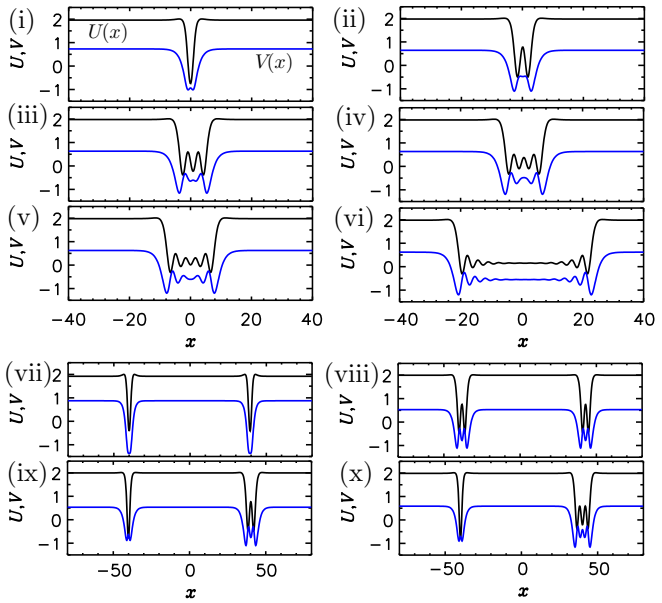

FIG. 10. Spatial profiles of the solutions represented in Fig. 8(a) for $\theta = 4$, showing $U(x)$ in black and $V(x)$ in blue. Panels (i)–(vi) correspond to one-soliton states [red branches in Figs. 8(a) and 9(a)], panels (vii) and (viii) to two-soliton states [reen branches in Figs. 8(a) and 9(b)], and panels (ix) and (x) to the branch of nonidentical two-soliton states [blue branch in Fig. 9(b)].

In finite systems the hole or one-soliton branch departs from $\rho \approx \rho_M$ when the maximum amplitude starts to decrease below A_0^t and the solution turns into a bright soliton sitting on top of A_0^b [Fig. 6, profile (iv)]. The branch then terminates at $\mathrm{SN}_{\mathrm{hom},1}$, where the amplitude of this soliton falls to zero. On an infinite domain the DS branches bifurcating from $\mathrm{SN}_{\mathrm{hom},2}$ and $\mathrm{SN}_{\mathrm{hom},1}$ remain distinct and do not connect up.

Figure 5 also shows the two-soliton branch (green curve). This branch consists of a pair of equidistant dark solitons within the periodic domain [Fig. 6, profiles (v)–(viii)]. The states on this branch can be viewed as one-pulse states on the half-domain and it is no surprise therefore that they follow the behavior of the one-pulse states shown in red. In fact, this is so for all n-soliton branches ($n \geqslant 3$, not shown), provided the solitons remain sufficiently well separated; finite-size effects push the bifurcation to these states farther from the saddle node at $\mathrm{SN}_{\mathrm{hom},2}$ as n increases, with similar behavior near $\mathrm{SN}_{\mathrm{hom},1}$.

Of particular interest is the third soliton branch [Fig. 5(b), blue curve]. This branch bifurcates from the vicinity of the first left fold on the two-soliton branch, labeled SN_{A}. This branch also undergoes collapsed snaking in the vicinity of ρ_M. The states on this branch start out as a two-soliton state consisting of a pair of (nearly) identical solitons [Fig. 6, profile (ix)] but only one of the two solitons broadens near ρ_M [Fig. 6, profiles (x) and (xi)]. The result is profile (xii) shown in Fig. 6 after translation by $L/4$. This state is seen to correspond to a single bright soliton, with a dip in the middle; numerical continuation shows that these states terminate on HSSs near $\mathrm{SN}_{\mathrm{hom},1}$ at the same location as the one-soliton branch (red curve). This new branch plays a particularly important role for $\theta > 2$, as discussed next.

C. Dark solitons for $\theta > 2$

For $\theta > 2$ the saddle node $\mathrm{SN}_{\mathrm{hom},1}$ becomes a RTBH point with spatial eigenvalues $\lambda_{1,2,3,4} = (0,0,\pm ik_0)$ and homoclinic orbits are exceptional [17,25]. However, in this case this point is preceded by a HH bifurcation on A_0^b, which gives rise to a branch of PSs. The PSs bifurcate subcritically (Fig. 8) but remain unstable throughout their existence range, despite the presence of a saddle node. This is the case for all values of the detuning θ we explored ($2.3 < \theta < 10$). Thus no bistability between PSs and A_0^b results and no snaking of bright DSs takes place [9,19]. Instead the bright solitons bifurcating from HH connect to the dark solitons originating at $\rho = \rho_t$, as we now describe.

Figure 8(a) shows the bifurcation diagram of the one-soliton states (red branch) for $\theta = 4$ obtained by numerically continuing the analytical prediction obtained in Eq. (19) away from $\mathrm{SN}_{\mathrm{hom},2}$. Figure 9(a) shows a detail of this branch. These states are initially unstable but as ρ increases these unstable one-soliton states grow in amplitude and acquire stability at

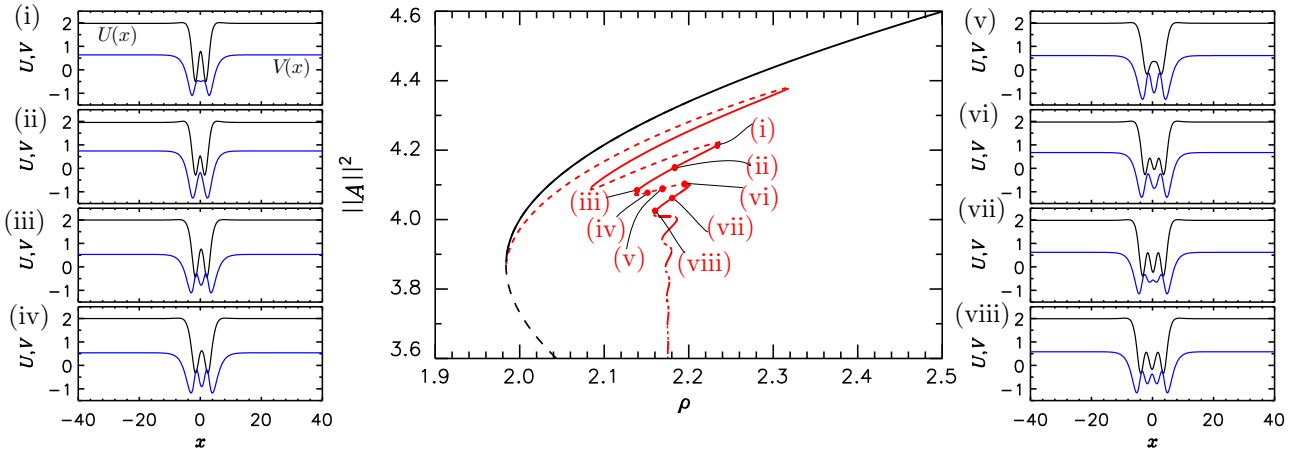

FIG. 11. Spatial profiles of the dark solitons near the upper end of the $\theta = 4$ one-soliton branch at locations indicated in the middle panel, showing that the splitting of the central peak (dip) in $(U(x),V(x))$, shown in black and red, respectively, occurs at different locations along the branch.

saddle node SN_1. The DS profile on this segment of the branch is shown in Fig. 10(i). This solution loses stability at SN_2 but starts to develop a spatial oscillation (SO) in the center; solutions of this type become stable at SN_3. An example of the resulting stable solution can be found in Fig. 10(ii). This process repeats in such a way that between successive saddle nodes on the left or right a new spatial oscillation is inserted in the center of the dark soliton profile and the soliton broadens, decreasing its L^2 norm. As a result, as one proceeds down the snaking branch the central peak (dip) repeatedly splits. Details of this process are shown in Fig. 11. The resulting behavior resembles in all aspects the phenomenon of defect-mediated snaking described in [29] except for the exponential shrinking of the region of existence of these states as the hole broadens. Consequently we refer to this behavior as collapsed defect-mediated snaking. Numerically the collapse occurs at $\rho = \rho_M \approx 2.175\,347\,9$. The DSs at this location correspond to broad holelike states of the type shown in Fig. 10(v). As in Sec. IV B further decrease in the norm signals that the two fronts connecting states A_0^t and A_0^b at ρ_M are starting to separate [Fig. 10(vi)]; this process continues, resulting in the bright soliton state shown in Fig. 12(iv); this state is shifted by $L/2$ relative to panels (i)–(vi) of Fig. 10. Thereafter the amplitude of the peak at $x = 0$ starts to decrease and the one-soliton branch departs from ρ_M, ultimately connecting to the branch of small amplitude PSs [Fig. 12(i)] that bifurcates subcritically from HH (see inset in Fig. 12, top panel).

Figure 8(a) also shows the two-soliton state (green line) that bifurcates from the vicinity of $SN_{hom,2}$ for $\theta = 4$ just as in the case $\theta = 1.95$. For $\theta > 2$ this second DS family plays a key role since it is responsible for providing the second of the two branches of localized states that are known to be associated with HH. Figures 9(b), 12, and 13 show how this happens. The green branch in Fig. 9(b) consists of states with identical equidistant solitons; like the one-soliton states, the two-soliton states proceed to develop internal oscillations [Figs. 10(vii) and 10(viii)]. These undergo a symmetry-breaking pitchfork bifurcation at SN_A giving rise to a branch of nonidentical solitons (in blue). One of these gradually acquires complex internal structure while the other remains unchanged. Figures 10(ix) and 10(x) show this state at the locations shown in Fig. 9(b), while Fig. 13(xii) shows a translation of such a two-soliton state by $L/4$. Figures 13(xii)–13(ix) and 12(xiv)–12(xi) show the subsequent evolution of this two-soliton state into a single wave packet with a minimum at its center $x = 0$. It is this state that connects to PSs at the same location as the corresponding wave packet (red) with a maximum at $x = 0$ that originates in the one-soliton state near $SN_{hom,2}$. In contrast, the two-soliton state that also appears near $SN_{hom,2}$ (green) terminates in a distinct bifurcation on the PS branch, as also shown in Fig. 12. All three branches undergo collapsed defect-mediated snaking in between. Evidently there are similar branches that bifurcate from other folds on the two-soliton branch (not shown).

We mention that as the domain length increases the termination point of the one-soliton (red line) and the nonidentical two-soliton branch (blue line) migrates towards HH and in the limit of an infinite domain the bright solitons bifurcate from A_0^b simultaneously with the PSs, exactly as predicted by the normal form for the spatial Hopf bifurcation with 1:1 resonance [24]. We also mention that, in principle, the Maxwell point ρ_M may collide with the saddle node of the PS branch (see [31] for details). However, we have determined that such a collision does not occur in the LLE and that the PS branch remains well separated from the collapsed snaking branches of dark solitons around ρ_M (at least in the parameter range $2.3 < \theta < 10$).

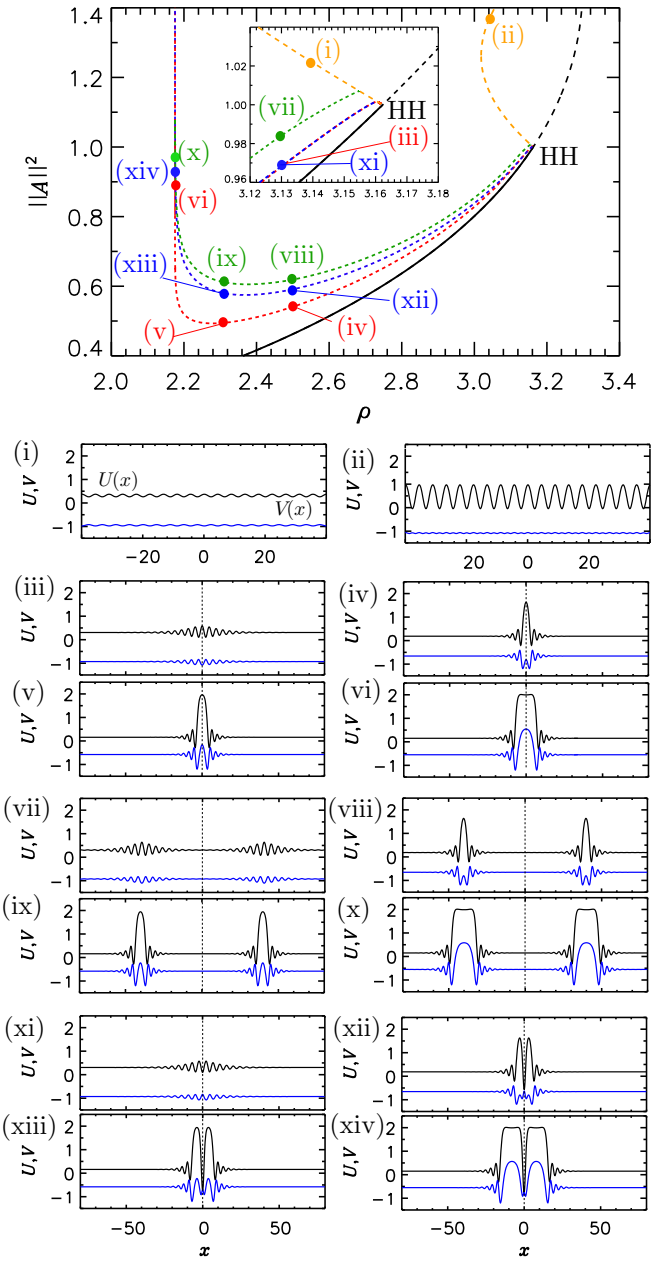

FIG. 12. Bifurcation diagram for $\theta = 4$ (top panel) showing the bifurcation of the three families of localized states (bright solitons) from the subcritical PS branch, together with sample solution profiles corresponding to the locations indicated in the top panel. States with maxima at $x = 0$ (red line) connect with the corresponding branch of dark solitons shown in Figs. 8(a) and 9(a) while states with minima at $x = 0$ (blue line) connect with the corresponding branch in Fig. 9(b). The states shown in green consist of two equidistant bright solitons and these connect to the corresponding branch in Fig. 9(b).

We turn, finally, to the structure of the spatial eigenvalues shown in Figs. 8(b) and 8(c). Panel (b) confirms that HH

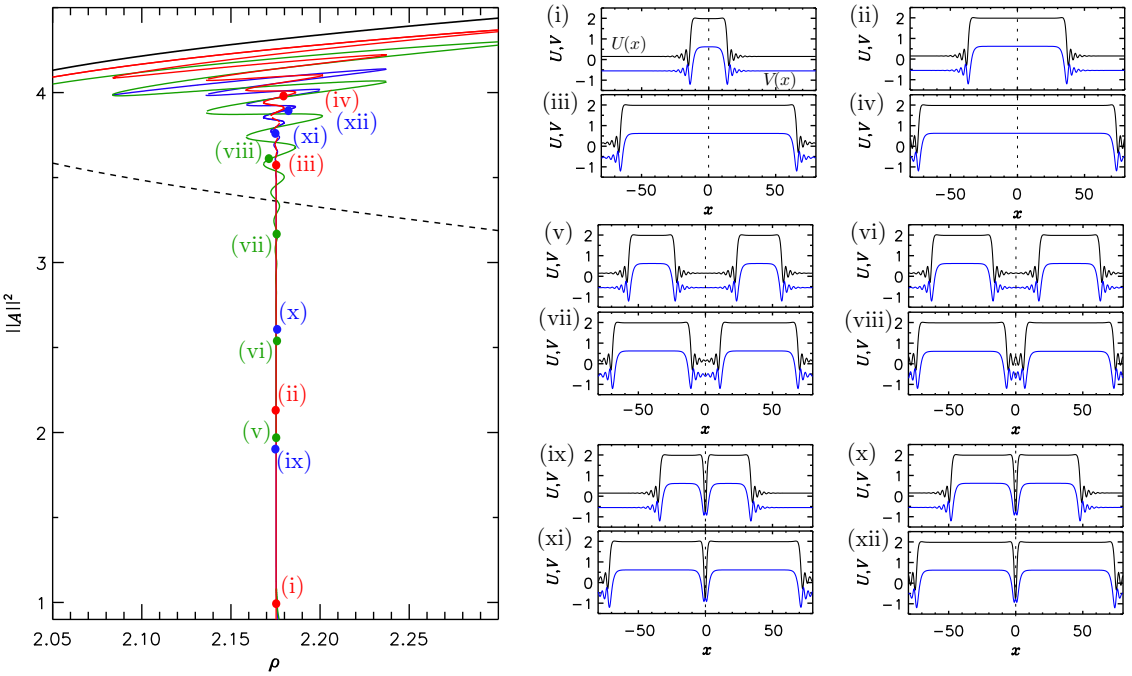

FIG. 13. Details of the profile transformation at $\theta = 4$ that changes two nonidentical dark solitons [blue branch in Fig. 9(b)] into a bright soliton with a minimum at its center $x = 0$, allowing it to connect to the PS at the same location as the one-soliton state [red branch in Fig. 9(a)] which evolves into a bright soliton with a maximum at its center $x = 0$. The two-soliton state consisting of two identical equidistant solitons [green branch in Fig. 9(b)] also terminates on the PS branch, but at a distinct location.

corresponds to a Hamiltonian-Hopf bifurcation in space. Panel (c) shows that at the termination point of the PS branch the HSS state A_0^m has two purely real and two purely imaginary spatial eigenvalues, indicating that SC corresponds to a global bifurcation in space and not a local bifurcation. Both HH and SC are formed in the process of unfolding the spatially reversible QZ bifurcation that takes place at $\mathrm{SN}_{\mathrm{hom},1}$ when $\theta = 2$.

D. Soliton location in the (θ, ρ) plane

Tracking each bifurcation point in the bifurcation diagram as a function of θ we obtain the (θ, ρ) parameter plane shown in Fig. 4. The green solid line represents a BD transition for $\theta < 2$ that turns into a HH bifurcation for $\theta > 2$. The saddle-node bifurcations determine the regions of existence of the different dark solitons shown previously. With increasing θ the region of existence of these states becomes broader [Figs. 14(a) and 14(b)]. In contrast, when θ decreases the branches of solutions with several SO progressively shrink, disappearing in a series of cusp bifurcations $C_1, \ldots, C_4$, as shown in Fig. 4.

We distinguish four main dynamical regions, labeled I–IV in the phase diagram in Fig. 4, on the basis of the existence of HSS and dark DSs:

(i) Region I: The bottom HSS A_0^b is stable. No dark DSs or top HSS A_0^t exist. This region spans the parameter space $\rho < \rho_{\mathrm{BD}}$ for $\theta < \sqrt{3}$ and $\rho < \rho_t$ for $\theta > \sqrt{3}$.

(ii) Region II: The bottom HSS A_0^b and top HSS A_0^t coexist and both are stable. No dark DSs are found. This region spans the parameter space $\rho_{\mathrm{SN}_1} < \rho < \rho_b$ for $\theta > \sqrt{3}$.

(iii) Region III: The top HSS A_0^t is stable. No dark DSs or bottom HSS A_0^b exist. This region spans the parameter space $\rho > \rho_{\mathrm{BD}}$ for $\theta < \sqrt{3}$ and $\rho > \rho_b$ for $\theta > \sqrt{3}$.

(iv) Region IV: The bottom HSS A_0^b and top HSS A_0^t are stable and coexist with (possibly unstable) dark DSs. This region spans the parameter space $\rho_t < \rho < \rho_{\mathrm{SN}_1}$ for $\theta > \sqrt{3}$. Here $\rho_t \equiv \rho_{\mathrm{SN}_{\mathrm{hom},2}}$ and $\rho_b \equiv \rho_{\mathrm{SN}_{\mathrm{hom},1}}$ as before.

Region IV is the main region of interest in this work. It can be further subdivided to reflect the locations of different types of DSs. In the next section, we refer to the region between SN_1 and SN_2, i.e., the region of existence of one-SO dark solitons, as subregion IV_1. Similarly, subregion IV_2 corresponds to two-SO dark solitons between SN_3 and SN_4 and so on. While both HSSs are stable in region IV, the stability of dark DSs in the various subregions depends on the parameter values (θ, ρ) as discussed next.

V. OSCILLATORY AND CHAOTIC DYNAMICS

We have seen that the range of values of the parameter ρ within which one finds dark solitons increases rapidly with increasing detuning θ, although the interval with stable stationary dark solitons is reduced by the presence of oscillatory instabilities that set in as θ increases (Fig. 14). These intervals of instability open up on the stable portions of the collapsed snaking branches, between pairs of supercritical Hopf bifurcations on either side. Consequently these instabilities lead to stable temporal oscillations resembling breathing of the individual solitons. To characterize the resulting dynamics we combine here linear stability analysis in time with direct integration of the LLE. We also compute secondary bifurcations of time-periodic states and point out that in appropriate regimes the LLE exhibits dynamics that are very similar to those exhibited by excitable systems.

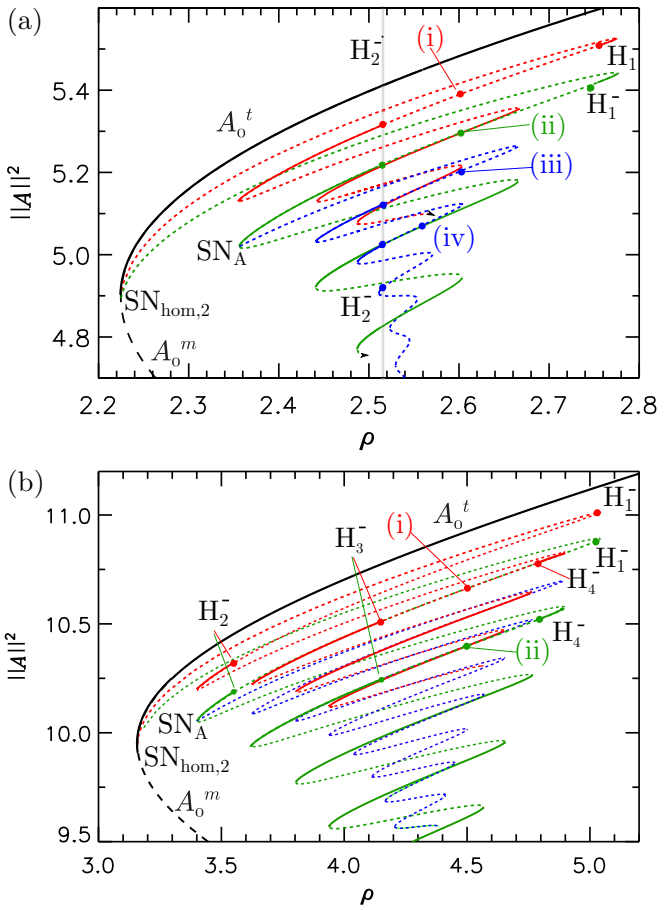

FIG. 14. Bifurcation diagram for (a) $\theta = 5$ and (b) $\theta = 10$ showing that the DSs are now unstable within intervals between back-to-back Hopf bifurcations. The Hopf bifurcations on the left [H_2^-, panel (a)] for the two-soliton states (green and blue lines) coincide with that of the one-soliton states (red line).

Figures 14(a) and 14(b) show that for both $\theta = 5$ and $\theta = 10$ the single dark soliton becomes unstable in a supercritical Hopf bifurcation (H_1^-) leading to an oscillatory state. Figure 15(i) shows the resulting state at location (i) in Fig. 14(a). The temporal oscillations disappear upon further decrease in ρ and do so in a reverse supercritical Hopf at H_2^-, thereby restoring the stability of the single dark soliton. For larger values of θ this behavior not only persists but the soliton with two spatial oscillations (SOs) also exhibits temporal oscillations between two back-to-back Hopf bifurcations [Fig. 14(b)]. An example of such an oscillatory two-SO dark soliton is shown in Fig. 16(i).

Figure 15(ii) shows the corresponding oscillation of the two-soliton state for $\theta = 5$ at location (ii) in Fig. 14(a). The solitons oscillate in phase but in a nonsinusoidal manner. Figures 15(iii) and 15(iv) show oscillations of a bound state of two nonidentical dark solitons at locations (iii) and (iv) in Fig. 14(a). In these states the simple dark soliton on the left oscillates in a periodic fashion while the structured dark soliton on the right remains essentially time independent. Figure 16(ii) shows a periodic oscillation of a two-soliton state for $\theta = 10$ corresponding to location (ii) in Fig. 14(b). The individual

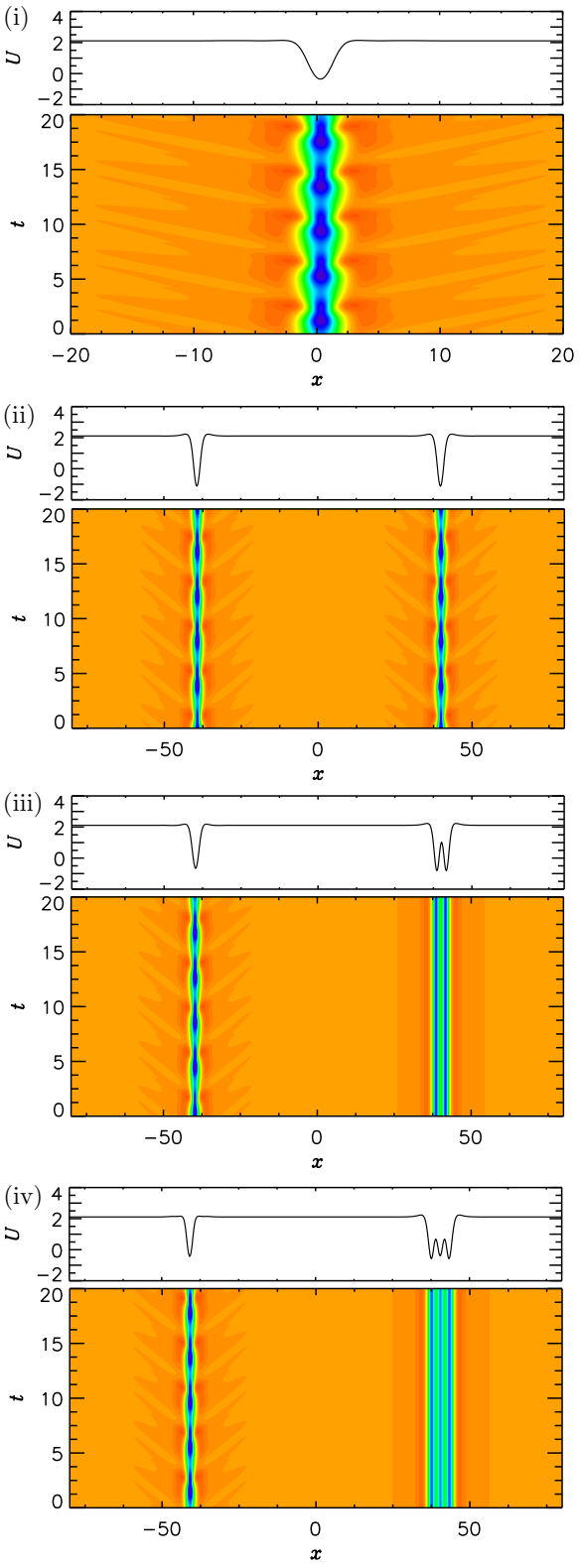

FIG. 15. (i) Oscillatory one-soliton state, (ii) oscillatory two-soliton state, (iii) a bound state of an oscillating and a stationary dark soliton, all computed for $\theta = 5$, $\rho = 2.6$. (iv) A similar state to panel (iii) but for $\theta = 5$, $\rho = 2.56$. The solutions are represented in a space-time plot of $U(x,t)$ with time increasing upwards. The profile at the final instant, $t = 20$, is shown above each space-time plot.

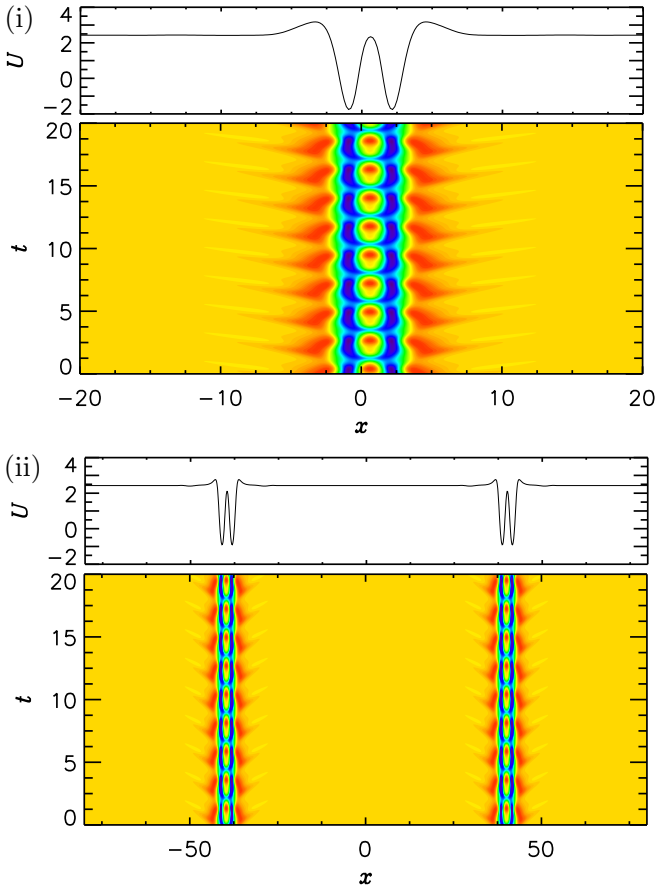

FIG. 16. (i) Oscillatory one-soliton state, and (ii) oscillatory two-soliton state, when $\theta = 10$, $\rho = 4.5$. The solutions are represented in a space-time plot of $U(x,t)$ with time increasing upwards. The profile at the final instant, $t = 20$, is shown above each space-time plot.

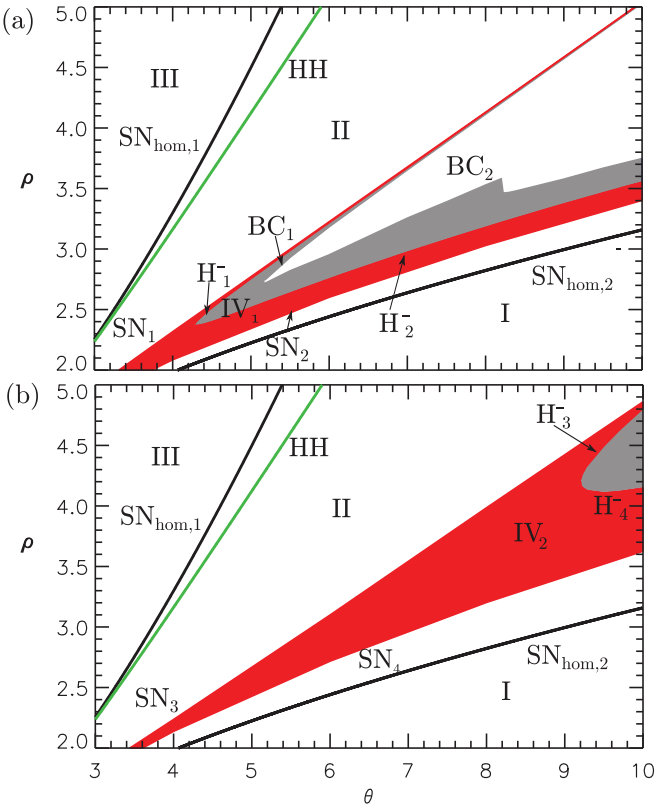

FIG. 17. The (θ,ρ) parameter space for normal dispersion ($\nu = -1$) showing the region of existence of (a) one-SO dark solitons and (b) two-SO dark solitons. The different bifurcations are labeled, with H_j^- indicating a supercritical Hopf bifurcation at location H_j. The red (gray) region corresponds to stable stationary (oscillatory) dark DSs.

solitons are structured and oscillate as in panel (i). Once again, both oscillate in phase.

We can complete the parameter space shown in Fig. 4 by adding the curves corresponding to the oscillatory instabilities at H_1^- and H_2^-. Figure 17 shows the parameter space with the curves corresponding to the temporal instabilities of the one-SO and two-SO dark solitons included; the saddle nodes of the remaining dark solitons are omitted in order to give a clearer understanding of this behavior. Bifurcation lines separating different dynamical regimes are labeled according to Fig. 14. With increasing θ the Hopf bifurcation H_1^- of the single dark DS approaches SN_1 and we see that both lines are almost tangent although, for the parameter values presented, they do not meet. The same scenario repeats for the Hopf bifurcation H_3^- of the two-SO state.

This scenario can be better understood by looking at Fig. 18 where several slices of Fig. 17 at different values of θ are shown. For stationary states we choose to plot the minimum $|A|_{\inf} := \min_x[|A(x)|]$ of the amplitude $A(x)$ instead of the L^2 norm to improve the clarity of the bifurcation diagram. For oscillatory solutions we plot the maxima and minima of this quantity, denoted by crosses. The diagram in Fig. 18(a) corresponds to a cut of Fig. 17 at $\theta = 4.6$. At this θ value the oscillatory state bifurcates from H_1^-, grows in amplitude as ρ decreases, before reconnecting to the stationary DS at H_2^- in a reverse Hopf bifurcation. For larger θ, the amplitude of the attracting periodic orbit between H_1^- and H_2^- increases, and at some point the orbit undergoes a period-doubling (PD) bifurcation, starting a route to a chaotic attractor. This happens already at $\theta = 5$ as can be seen in Fig. 18(b). At $\theta = 5.2$ [Fig. 18(c)] the chaotic attractor touches the saddle branch S corresponding to unstable dark solitons and disappears through a boundary crisis (BC) [32].

Let us discuss this process in detail for the attracting periodic orbit emerging from H_2^- (the case of H_1^- is analogous). In Fig. 19 we show a zoom of the diagram in Fig. 18(c) close to BC_2 and in Fig. 20 a series of panels characterizing the attracting periodic orbit at different values of ρ is shown. From left to right we show a series of time traces showing the oscillation in the minimum amplitude $|A|_{\inf}$ of the soliton, the Fourier transform of these time traces, a two-dimensional phase space projection onto $(U(x_0,t),V(x_0,t))$, x_0 being the position of the center of the structure, and a zoom of the phase space. Figure 20(a) corresponds to the situation at $\rho = 2.702\,48$ in Fig. 19 labeled with (a). As we can see from the time trace and the frequency spectrum, the periodic orbit has a single period. In the phase space shown in Fig. 20 we observe a fixed point corresponding to A_0^t, a saddle point corresponding to the unstable dark soliton denoted by

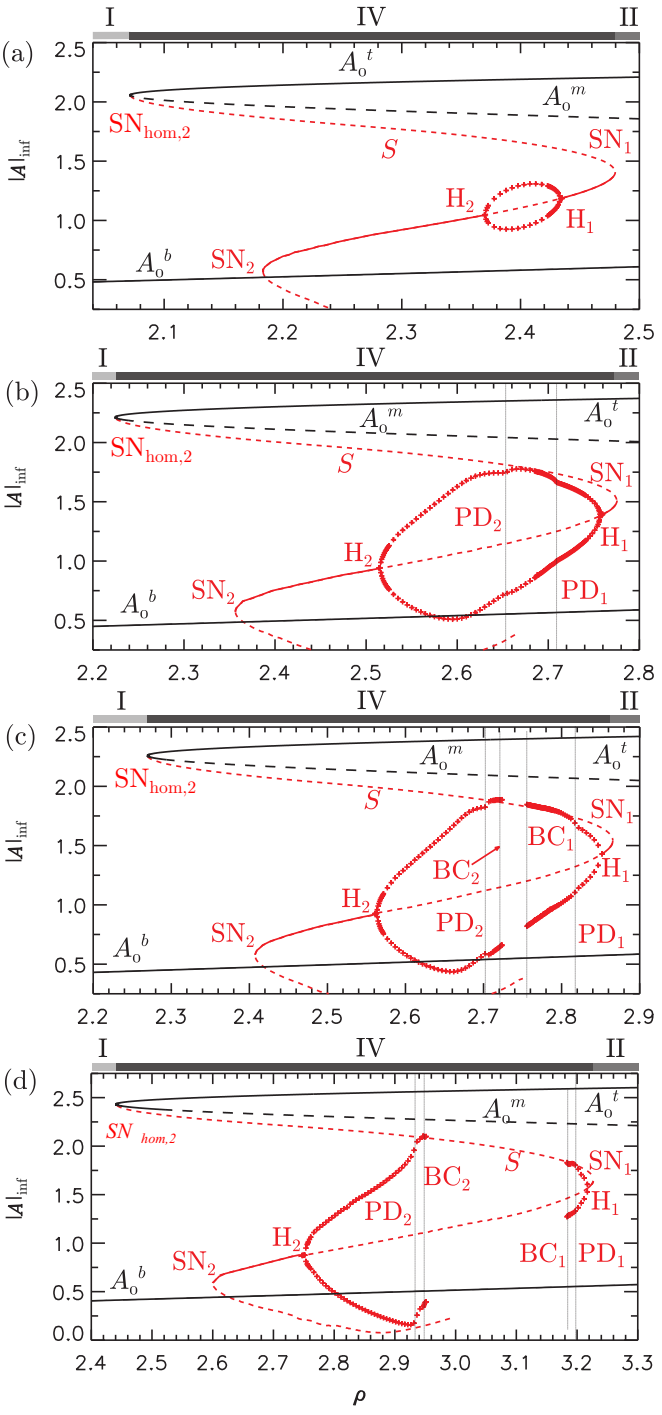

FIG. 18. Bifurcation diagrams corresponding to different slices of the parameter space in Fig. 17 plotted using $|A|_{\rm inf}$ as a measure of the amplitude. Solid (dashed) lines correspond to stable (unstable) structures, and red (black) colors correspond to one-SO dark DSs (HSS). The red crosses represent maxima and minima of the amplitude of the oscillatory dark DSs. The gray labeled bars above each panel show the extent of the regions I, II, and IV. (a) $\theta = 4.6$, (b) $\theta = 5$, (c) $\theta = 5.2$, (d) $\theta = 5.5$.

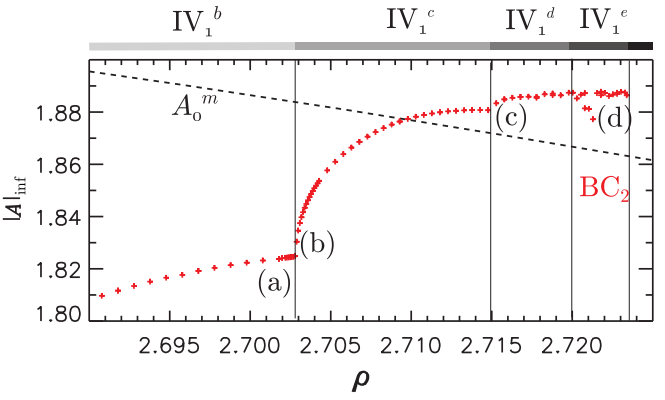

FIG. 19. Detail of the bifurcation diagram of Fig. 18(c) for $\theta = 5.2$ close to the BC_2 point. Vertical lines separate period-1 oscillations (region IV_1^b), period-2 oscillations (region IV_1^c), period-4 oscillations (region IV_1^d), and temporal chaos in region IV_1^e. Lines and markers in red (black) correspond to dark DSs (HSS). Labels from (a) to (d) correspond to the dynamics shown in Fig. 20.

S and a periodic orbit corresponding to a periodic oscillation in time, localized in space. For this value of ρ the saddle S is far from the periodic orbit. For $\rho = 2.703\,58$ [panel (b) corresponding to label (b) in Fig. 19] the time trace and the spectrum reveal that the periodic orbit has period 2 as can also be discerned from the phase-space projection. In Fig. 20(c), for $\rho = 2.715\,28$, the periodic orbit has just suffered another period doubling resulting in a periodic orbit with period 4. Finally, Fig. 20(d) shows the situation for $\rho = 2.721\,78$, where the orbit has become a chaotic attractor. At this parameter value the system is very close to the boundary crisis BC_2 as can appreciated from the near tangency between S and the chaotic attractor. Once S touches the attractor, the latter disappears and only A_0^t and A_0^b remain as attractors of the system. The same occurs to the periodic orbits appearing at H_1^-. Using time simulations we were able to estimate the position of the boundary crises BC_1 and BC_2 in parameter space, labeled in Fig. 17(a). From Figs. 18(c) and 18(d) we can see that at the same time as BC_1 moves toward H_1^-, H_1^- itself approaches SN_1 and therefore that the region of existence of oscillatory DSs shrinks. This behavior can also be seen in Fig. 17(a).

At this point we can differentiate five main dynamical subregions related to region IV_1, i.e., the one-SO dark soliton, namely

(i) IV_1^a: the one-SO dark soliton is stable;
(ii) IV_1^b: the soliton oscillates with a single period;
(iii) IV_1^c: the soliton oscillates with period 2;
(iv) IV_1^d: the soliton oscillates with period 4;
(v) IV_1^e: region of temporal chaos bounded by a boundary crisis (BC_2).

The region IV_2 of two-SO dark solitons has the same sequence of subregions $IV_2^a, \ldots, IV_2^e$, etc.

Close to BC_2 (respectively, BC_1) the system can exhibit behavior reminiscent of excitability [33]. Here the stable manifold of the saddle soliton S acts as a separatrix or threshold in the sense that perturbations of A_0^t across that threshold do not relax immediately to A_0^t but lead first to a large excursion in phase space before relaxing to A_0^t. In this case the excursion corresponds to what is known as a chaotic transient, where the system exhibits transient behavior reminiscent of the chaotic attractor at lower values of ρ [10,34]. In Figs. 21(a) and 21(b) we show two examples of this kind of transient dynamics. We choose a value of ρ close to BC_2, namely $\rho = 2.7235$,

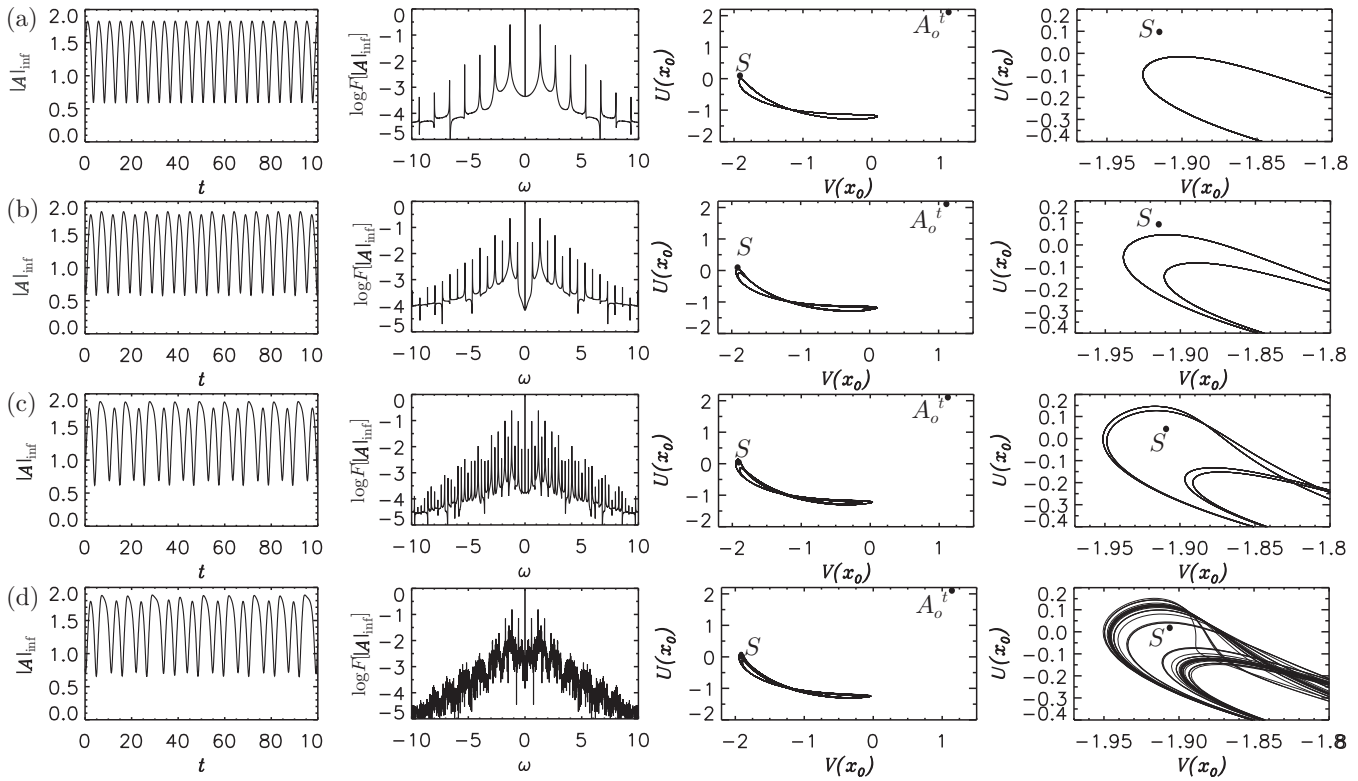

FIG. 20. Route to temporal chaos for $\theta = 5.2$. Panels (a)–(d) represent the transition from (a) period-1 oscillations to (d) temporal chaos, corresponding to the labels in Fig. 19. From left to right: temporal trace of $|A|_{\inf}$, its frequency spectrum that allows us to differentiate between the different types of temporal periodicity, a portion of the phase space containing A_0^t, S and the periodic attractors, and a zoom of the latter where we can appreciate the proximity of the solution trajectory to S. (a) $\rho = 2.702\,48$ (period 1), (b) $\rho = 2.703\,58$ (period 2), (c) $\rho = 2.715\,28$ (period 4), (d) $\rho = 2.721\,78$ (temporal chaos).

and modify the parameter ρ for a brief instant using a Gaussian profile of width σ and height h using the instantaneous transformation $\rho \mapsto \rho + h(t)\exp[-(x - L/2)^2/\sigma^2]$, where $\rho = 2.7235$ and $\sigma = 0.781\,250$ with $h(t) = -2.55$ for $10 \leqslant t \leqslant 15$ and $h = 0$ elsewhere [35]. As shown in Fig. 21(a) such a perturbation of A_0^t allows the system to explore the chaotic attractor before returning to the rest state. In contrast, in Fig. 21(b) the system explores just one loop of the orbit before returning to the rest state.

VI. DISCUSSION

In this work we have presented a comprehensive overview of the dynamics of the LLE in the normal dispersion regime.

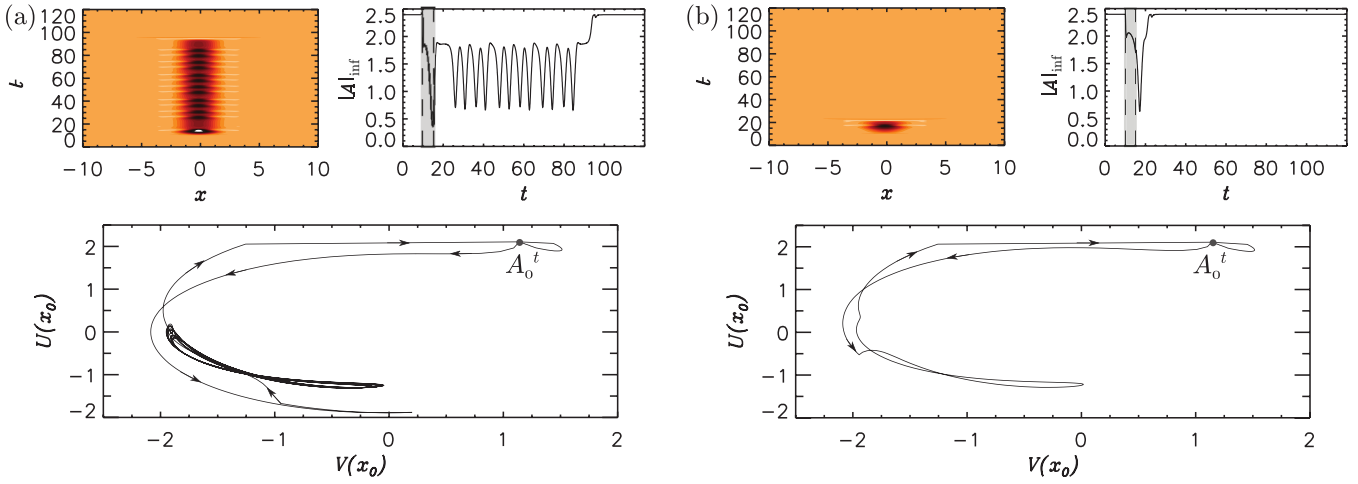

FIG. 21. Chaotic transient dynamics for $\theta = 5.2$: (a) A chaotic transient is generated when A_0^t is temporally perturbed with a Gaussian perturbation of height $h = -2.55$ (see gray area in time traces); (b) a similar excursion for $h = -3.4431$. In both (a) and (b) the top left panels represent space-time plots of the temporal evolution of the field $U(x,t)$, the top right panels show the time series of the norm $|A|_{\inf}$ and the bottom panels show a projection of the phase-space trajectory.

The bifurcation structure of dark dissipative solitons (DSs), their stability and the regions of their existence were determined. Three families of dark solitons, the one-soliton and two different types of two-soliton states, located on three intertwined branches undergoing collapsed snaking in the vicinity of the same Maxwell point, were identified. The one-soliton states bifurcate from the top left fold of an S-shaped branch of spatially homogeneous states and terminate either on the lower homogeneous steady-state (HSS) branch in a Hamiltonian-Hopf (HH) (equivalently, modulational instability) or at the bottom right fold, depending on the detuning parameter θ. On a periodic domain of finite spatial period, these bifurcations are slightly displaced from the folds, and in the case of the HH bifurcation to finite amplitude on the branch of periodic states created in this bifurcation. The two-soliton states consisting of a pair of identical equidistant solitons in the domain follow a similar branch but branch off the HSS farther from the folds. This is a finite-size effect: these states behave like the one-soliton states on a periodic domain with half the domain length. The third branch consists of a pair of nonidentical solitons and plays a key role: this branch bifurcates from the branch of identical two-soliton states in a pitchfork bifurcation; as one follows this branch to lower L^2 norm these states undergo a remarkable metamorphosis into a bright soliton with a minimum at its center that allows it to terminate on the periodic states created in the HH bifurcation at the same location as the one-soliton states, as demanded by theory. The details of this transition are captured in Figs. 12 and 13. Related behavior likely occurs in the Swift-Hohenberg equation as well (see Fig. 19 of [36]).

At yet higher values of the detuning parameter θ we found that the localized states undergo oscillatory instabilities, and at a certain point a period-doubling bifurcation initiates a period-doubling cascade into chaos. We have used this observation to determine the regions in parameter space where different stationary and dynamical states coexist.

We have shown that the bifurcations that organize the spatial dynamics undergo an important transition at a quadruple-zero (QZ) point, which occurs at $(\theta,\rho)=(2,\sqrt{2})$. Here, in the normal dispersion regime, the Belyakov-Devaney (BD) transition turns into an HH bifurcation as the detuning θ increases through $\theta=2$. For $\theta>2$ a spatially periodic pattern bifurcates subcritically from the bottom homogeneous state at this HH bifurcation. These periodic solutions were found to be unstable, and hence no stable bright DSs were found. However, the saddle-node bifurcation of the top homogeneous solution remains a reversible Takens-Bogdanov (RTB) bifurcation for all $\theta>\sqrt{3}$. This observation explains the existence of multiple families of dark DSs in this regime, and their organization in the so-called *collapsed snaking* structure [17,29]. As mentioned, these dark DSs undergo various dynamical instabilities for larger values of the detuning θ.

The bifurcation scenario is largely reversed in the case of anomalous dispersion, where the same QZ point plays an equally important role, but now the HH bifurcation turns into a BD bifurcation when $\theta>2$ [11,12]. Moreover, the top homogeneous solution is now always unstable and the upper fold never corresponds to a RTB bifurcation. This reverse character of the bifurcation points has important consequences. First, dark DSs no longer exist, although the inclusion of additional, higher-order dispersion can stabilize the top homogeneous solution and hence lead to stable dark DSs [37]. Second, for $41/30<\theta<2$, a stable periodic solution coexists with the stable bottom homogeneous solution giving rise to bright DSs that are organized in a homoclinic snaking structure [9,19]. For $\theta>2$, however, the snaking structure of such bright DSs breaks down, as will be reported elsewhere. Finally, despite these differences in the regions of existence of dark and bright DSs in the normal vs anomalous dispersion regime, the temporal dynamics of the existing solutions are very similar at higher values of the detuning θ. Here, for normal dispersion, we reported the existence of oscillatory and chaotic dynamics of dark DSs as the detuning is increased. The same dynamical instabilities have been observed in the case of anomalous dispersion at high values of θ, but this time for bright DSs [10,11]. This suggests that the unfolding of the dynamics can be related to the same type of bifurcation point in both cases.

VII. CONCLUDING REMARKS

The analysis of this paper provides a detailed map of the regions of existence and stability of dark DSs, which could serve as a guide for experimentalists to target particular DS solutions. We showed that dark DSs exist only in a well-defined zone within the wider region of bistability between two stable homogeneous solutions. Within this zone, dark DSs are organized in a bifurcation structure called a *collapsed snaking* structure. The word "collapsed" refers to the fact that the region of existence of dark DSs shrinks exponentially with increasing number of spatial oscillations (SOs) in the soliton profile (Fig. 8). The collapse of the snaking structure implies that DSs with many SOs can only be found at the Maxwell point ρ_M, a fact that favors the observation of DSs with a single SO over that of broader DS with many SOs.

Although such a collapsed snaking structure persists for higher values of the detuning θ, we also showed that narrow dark DSs with a low number of SOs destabilize first as θ increases (Fig. 14) and start to oscillate in time. Therefore, at higher values of θ stable dark DSs found experimentally will most likely have an intermediate number of SOs. Our general analysis of the multistability of dark DSs may also explain the numerical observations in Ref. [12], where it was shown that the pulse profile of dark DSs becomes more distorted as the detuning increases. This may be due to the fact that stable dark DSs with a larger number of SOs are more likely to be found for higher values of the detuning.

The LLE has recently attracted renewed interest owing to the strong correspondence between Kerr temporal solitons and frequency combs (FCs) [38]. FCs consist of a set of equidistant spectral lines that can be used to measure light frequencies and hence time intervals more easily and precisely than ever before [39]. For this reason FCs open up a large variety of applications ranging from optical clocks to astrophysics [39]. We explore the consequences of the present analysis for FC technology in a companion paper [15].

As shown in Fig. 4, in the normal dispersion regime rather large values of the detuning θ and pump power ρ are required to obtain a sufficiently wide region of dark DSs (region IV) to observe such states experimentally. However, in recent years,

the FC community has become increasingly successful at reaching the required values of pump power and detuning. As a result, dark DSs with different numbers of spatial oscillations (SOs) in their center (see, e.g., Fig. 10) have been observed in experiments [13]. In Ref. [13] dark DSs were found using a normalized pump power $\rho \approx 2.5$ and normalized detuning $\theta \approx 5$. Figures 17 and 18 show that around these parameter values one can indeed find dark DSs with different numbers of SOs that can undergo oscillatory instabilities.

ACKNOWLEDGMENTS

This research was supported by the Research Foundation–Flanders (FWO-Vlaanderen) (P.P. and L.G.), by the Junior Mobility Programme (JuMo) of the KU Leuven (L.G.), by the Belgian Science Policy Office (BelSPO) under Grant No. IAP 7-35 (P.P. and L.G.), by the Research Council of the Vrije Universiteit Brussel (P.P. and L.G.), by the Spanish MINECO and FEDER under Grant Intense@Cosyp (FIS2012-30634) (D.G.), and by the National Science Foundation under Grant No. DMS-1211953 (E.K.). We thank S. Coen and F. Leo for valuable discussions.

APPENDIX

In this Appendix we present details of the weakly nonlinear analysis near the RTB bifurcation at $\mathrm{SN}_{\mathrm{hom},2}$ used to obtain analytically the spatially localized state in Eq. (19). These states are solutions of the ODE system defined by

$$\begin{aligned} -\nu\frac{d^2V}{dx^2} - U + \theta V - V(U^2+V^2) + \rho = 0, \\ \nu\frac{d^2U}{dx^2} - V - \theta U + U(U^2+V^2) = 0. \end{aligned} \tag{A1}$$

The bifurcation $\mathrm{SN}_{\mathrm{hom},2}$ takes place at

$$I_t = \frac{1}{3}(2\theta + \sqrt{\theta^2-3}) \tag{A2}$$

and we consider a Taylor series expansion of ρ around I_t:

$$\begin{aligned} \rho(I_0) = \underbrace{\rho(I_t)}_{\rho_t} + \underbrace{\left(\frac{d\rho}{dI_0}\right)_{I_t}}_{=0}(I_0 - I_t) \\ + \underbrace{\frac{1}{2}\left(\frac{d^2\rho}{dI_0^2}\right)_{I_t}}_{\delta}\underbrace{(I_0-I_t)^2}_{\epsilon^2} + \cdots \end{aligned} \tag{A3}$$

with

$$\rho_t = \sqrt{I_t^3 - 2\theta I_t^2 + (1+\theta^2)I_t}. \tag{A4}$$

Because ρ_t has a minimum at I_t, we have

$$\left(\frac{d\rho}{dI_0}\right)_{I_t} = 0,$$

$$\delta \equiv \frac{1}{2}\left(\frac{d^2\rho}{dI_0^2}\right)_{I_t} = \frac{\sqrt{\theta^2-3}}{2\rho_t} > 0.$$

We define a small parameter ϵ in terms of ρ,

$$\epsilon = \sqrt{\frac{\rho-\rho_t}{\delta}}, \tag{A5}$$

and use ϵ as an expansion parameter.

The localized states of interest can be written in the form

$$\begin{bmatrix} U \\ V \end{bmatrix} = \begin{bmatrix} U \\ V \end{bmatrix}^* + \begin{bmatrix} u \\ v \end{bmatrix}, \tag{A6}$$

with the spatially uniform states HSS given by

$$\begin{bmatrix} U \\ V \end{bmatrix}^* = \begin{bmatrix} U_t \\ V_t \end{bmatrix} + \epsilon\begin{bmatrix} U_1 \\ V_1 \end{bmatrix} + \epsilon^2\begin{bmatrix} U_2 \\ V_2 \end{bmatrix} + \cdots \tag{A7}$$

and the space-dependent terms by

$$\begin{bmatrix} u \\ v \end{bmatrix} = \epsilon\begin{bmatrix} u_1 \\ v_1 \end{bmatrix} + \epsilon^2\begin{bmatrix} u_2 \\ v_2 \end{bmatrix} + \cdots. \tag{A8}$$

We allow the fields u_1, v_1, u_2, and v_2 to depend on the slow variable $X \equiv \sqrt{\epsilon}x$. We first calculate the HSS terms and then do the same for the space-dependent terms.

1. Asymptotics for the uniform states

Inserting the ansatz (A7) in Eq. (A1), we obtain the correction to the HSS A_0 at any order in ϵ.

At order $O(\epsilon^0)$ we obtain expressions for U_t and V_t as a function of θ. At order $O(\epsilon^1)$ we have

$$L\begin{bmatrix} U_1 \\ V_1 \end{bmatrix} = \begin{bmatrix} 0 \\ 0 \end{bmatrix}, \tag{A9}$$

where

$$L = \begin{bmatrix} 0 & 0 \\ -(\theta - I_t - 2U_t^2) & -2 \end{bmatrix} \tag{A10}$$

is a singular linear operator. Equation (A9) has an infinite number of solutions that can be written in the form

$$\begin{bmatrix} U_1 \\ V_1 \end{bmatrix} = \mu\begin{bmatrix} 1 \\ \eta \end{bmatrix}, \tag{A11}$$

where

$$\eta = -\frac{1}{2}(\theta - I_t - 2U_t^2) \tag{A12}$$

and μ is obtained by solving the $O(\epsilon^2)$ system. At this order we obtain the equation

$$L\begin{bmatrix} U_2 \\ V_2 \end{bmatrix} = \begin{bmatrix} 2U_1V_1U_t + (2V_1^2 + I_1)V_t - \delta \\ -(2U_1^2 + I_1)U_t - 2V_1U_1V_t \end{bmatrix}, \tag{A13}$$

where $I_1 \equiv U_1^2 + V_1^2$. Because L is singular, the previous equation has no solution unless a solvability condition is satisfied. This condition is given by

$$\mu = \sqrt{\frac{\delta}{3\eta^2V_t + 2\eta U_t + V_t}}. \tag{A14}$$

2. Asymptotics for the space-dependent states

To calculate the space-dependent component of the weakly nonlinear state, we proceed in the same fashion. We insert the

full ansatz for the asymptotic state, namely Eq. (A6), into the system (A1) and obtain, at order $O(\epsilon^1)$,

$$\underbrace{L\begin{bmatrix}U_1\\V_1\end{bmatrix}}_{=0}+L\begin{bmatrix}u_1\\v_1\end{bmatrix}=\begin{bmatrix}0\\0\end{bmatrix}, \tag{A15}$$

where the first term on the left-hand side vanishes. The general solution of this equation is

$$\begin{bmatrix}u_1\\v_1\end{bmatrix}=\begin{bmatrix}U_1\\V_1\end{bmatrix}\psi(X), \tag{A16}$$

with $\psi(X)$ a function to be determined at the next order.

At order $O(\epsilon^2)$

$$L\begin{bmatrix}u_2\\v_2\end{bmatrix}=-\mathcal{P}_1\begin{bmatrix}u_1\\v_1\end{bmatrix}-\mathcal{P}_2\begin{bmatrix}U_t\\V_t\end{bmatrix}, \tag{A17}$$

with the linear operators

$$\mathcal{P}_1=\begin{bmatrix}-(2U_tV_1+2U_1V_t) & -\left(\nu\partial_X^2+6V_tV_1+2U_tU_1\right)\\ \nu\partial_X^2+6U_tU_1+2V_tV_1 & 2V_tU_1+2U_tV_1\end{bmatrix} \tag{A18}$$

and

$$\mathcal{P}_2=\begin{bmatrix}-2v_1u_1 & -\left(3v_1^2+u_1^2\right)\\ 3u_1^2+v_1^2 & 2v_1u_1\end{bmatrix}. \tag{A19}$$

Because L is singular, Eq. (A17) has no solution unless another solvability condition is satisfied. In the present case, this condition reads

$$[1\,0]\mathcal{P}_1\begin{bmatrix}u_1\\v_1\end{bmatrix}+[1\,0]\mathcal{P}_2\begin{bmatrix}U_t\\V_t\end{bmatrix}=0. \tag{A20}$$

After some algebra, Eq. (A20) reduces to an ordinary differential equation for $\psi(X)$,

$$\alpha_1\psi''(X)+\alpha_2\psi(X)+\alpha_3\psi^2(X)=0, \tag{A21}$$

where

$$\alpha_1=-\nu V_1,\quad \alpha_2=-2\delta,\quad \alpha_3=-\delta. \tag{A22}$$

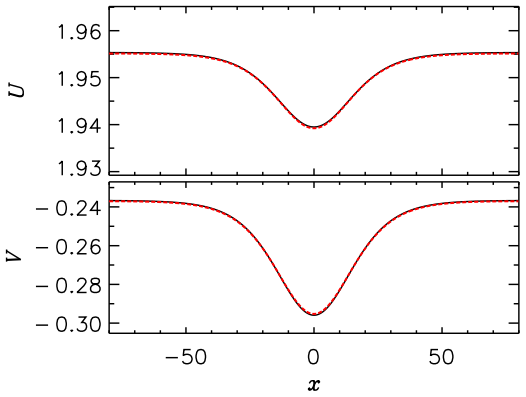

FIG. 22. Asymptotic and exact hole solutions $A(x)\equiv U(x)+iV(x)$ close to $\mathrm{SN}_{\mathrm{hom},2}$ for $\theta=4$ and $\rho=1.983\,88$. The black solid line shows the asymptotic solution for comparison with the numerically exact solution obtained by numerical continuation (red dashed line). The two lines are indistinguishable.

This equation has solutions homoclinic to $\psi=0$ given by

$$\psi(X)=-3\mathrm{sech}^2\left(\frac{1}{2}\sqrt{-\frac{\alpha_2}{\alpha_1}}(X-X_0)\right), \tag{A23}$$

representing a hole in the spatially uniform state located at $X=X_0$, hereafter at $X=0$. Since $X\equiv\sqrt{\epsilon}x$ and $\epsilon\equiv\sqrt{\frac{\rho-\rho_t}{\delta}}$ the corresponding first-order spatial correction is given by

$$\begin{bmatrix}u_1\\v_1\end{bmatrix}=-3\mu\begin{bmatrix}1\\\eta\end{bmatrix}\mathrm{sech}^2\left[\frac{1}{2}\sqrt{-\frac{\alpha_2}{\alpha_1}}\left(\frac{\rho-\rho_t}{\delta}\right)^{1/4}x\right]. \tag{A24}$$

The resulting asymptotic solution for $\theta=4$ and $\rho=1.983\,88$ is shown in Fig. 22 (black solid lines). The corresponding numerically exact solution, obtained using numerical continuation, is shown in red dashed lines. The agreement is excellent.

For $\sqrt{3}<\theta<2$ the saddle node $\mathrm{SN}_{\mathrm{hom},1}$ is also a RTB bifurcation and the same asymptotic calculation can therefore be used to compute the DSs present near this bifurcation. A related calculation can be used to compute the DS profiles near the point HH [17].

[1] *Dissipative Solitons*, Lecture Notes in Physics No. 661, edited by N. Akhmediev and A. Ankiewicz (Springer, New York, 2005); *Dissipative Solitons: From Optics to Biology and Medicine*, Lecture Notes in Physics No. 751, edited by N. Akhmediev and A. Ankiewicz (Springer, New York, 2008).

[2] J. E. Pearson, Science **261**, 189 (1993); K. J. Lee, W. D. McCormick, Q. Ouyang, and H. L. Swinney, *ibid.* **261**, 192 (1993).

[3] I. Müller, E. Ammelt, and H. G. Purwins, Phys. Rev. Lett. **82**, 3428 (1999).

[4] O. Thual and S. Fauve, J. Phys. (France) **49**, 1829 (1988).

[5] W. A. Macfadyen, Geogr. J. **116**, 199 (1950).

[6] L. A. Lugiato, IEEE J. Quantum Electron. **39**, 193 (2003); M. Tlidi, P. Mandel, and R. Lefever, Phys. Rev. Lett. **73**, 640 (1994); B. Schäpers, M. Feldmann, T. Ackemann, and W. Lange, *ibid.* **85**, 748 (2000); S. Barland, J. R. Tredicce, M. Brambilla, L. A. Lugiato, S. Balle, M. Giudici, T. Maggipinto, L. Spinelli, G. Tissoni, T. Knodl, M. Miller, and R. Jager, Nature (London) **419**, 699 (2002); W. J. Firth and C. O. Weiss, Opt. Photon. News **13**, 55 (2002); F. Pedaci, S. Barland, E. Caboche, P. Genevet, M. Giudici, J. R. Tredicce, T. Ackemann, A. Scroggie, W. Firth, G. L. Oppo, G. Tissoni, and R. Jaeger, Appl. Phys. Lett. **92**, 011101 (2008); V. Odent, M. Taki, and E. Louvergneaux, New J. Phys. **13**, 113026 (2011).

[7] F. Leo, S. Coen, P. Kockaert, S. P. Gorza, P. Emplit, and M. Haelterman, Nat. Photon. **4**, 471 (2010).

[8] L. A. Lugiato and R. Lefever, Phys. Rev. Lett. **58**, 2209 (1987).

[9] D. Gomila, A. J. Scroggie, and W. J. Firth, Phys. D (Amsterdam) **227**, 70 (2007).

[10] F. Leo, L. Gelens, P. Emplit, M. Haelterman, and S. Coen, Opt. Express **21**, 9180 (2013).

[11] P. Parra-Rivas, D. Gomila, M. A. Matías, S. Coen, and L. Gelens, Phys. Rev. A **89**, 043813 (2014).

[12] C. Godey, I. V. Balakireva, A. Coillet, and Y. K. Chembo, Phys. Rev. A **89**, 063814 (2014).

[13] X. Xue, Y. Xuan, Y. Liu, P.-H. Wang, S. Chen, J. Wang, D. E. Leaird, M. Qi, and A. M. Weiner, Nat. Photon. **9**, 594 (2015).

[14] V. E. Lobanov, G. Lihachev, T. J. Kippenberg, and M. L. Gorodetsky, Opt. Expr. **23**, 7713 (2015).

[15] P. Parra-Rivas, D. Gomila, E. Knobloch, S. Coen, and L. Gelens, Opt. Lett. **41**, 2402 (2016).

[16] M. Haelterman, S. Trillo, and S. Wabnitz, Opt. Commun. **91**, 401 (1992).

[17] J. Burke, A. Yochelis, and E. Knobloch, SIAM J. Appl. Dyn. Syst. **7**, 651 (2008).

[18] M. Haragus and G. Iooss, *Local Bifurcations, Center Manifolds, and Normal Forms in Infinite-Dimensional Dynamical Systems* (Springer, Berlin, 2011).

[19] A. R. Champneys, Phys. D (Amsterdam) **112**, 158 (1998).

[20] P. Colet, M. A. Matías, L. Gelens, and D. Gomila, Phys. Rev. E **89**, 012914 (2014); L. Gelens, M. A. Matías, D. Gomila, T. Dorissen, and P. Colet, *ibid.* **89**, 012915 (2014).

[21] R. Devaney, Trans. Am. Math. Soc. **218**, 89 (1976).

[22] A. J. Homburg and B. Sandstede, in *Handbook of Dynamical Systems*, edited by B. Hasselblatt, H. Broer, and F. Takens (North-Holland, Amsterdam, 2010), Chap. 8, pp. 379–524.

[23] E. Knobloch, Annu. Rev. Condens. Matter Phys. **6**, 325 (2015).

[24] G. Iooss and M. C. Pérouème, J. Diff. Eqs. **102**, 62 (1993).

[25] K. Kolossovski, A. R. Champneys, A. V. Buryak, and R. A. Sammut, Phys. D (Amsterdam) **171**, 153 (2002).

[26] E. L. Allgower and K. Georg, *Numerical Continuation Methods: An Introduction* (Springer, Berlin, 1990).

[27] Y. S. Kivshar, V. V. Afansjev, and A. W. Snyder, Opt. Commun. **126**, 348 (1996); H. E. Nistazakis, D. J. Frantzeskakis, P. S. Balourdos, A. Tsigopoulos, and B. A. Malomed, Phys. Lett. **A278**, 68 (2000); M. Crosta, A. Fratalocchi, and S. Trillo, Phys. Rev. A **84**, 063809 (2011).

[28] J. Knobloch and T. Wagenknecht, Phys. D (Amsterdam) **206**, 82 (2005).

[29] Y.-P. Ma, J. Burke, and E. Knobloch, Phys. D (Amsterdam) **239**, 1867 (2010).

[30] A. Yochelis, J. Burke, and E. Knobloch, Phys. Rev. Lett. **97**, 254501 (2006).

[31] A. R. Champneys, E. Knobloch, Y.-P. Ma, and T. Wagenknecht, SIAM J. Appl. Dyn. Syst. **11**, 1583 (2012).

[32] R. Hilborn, *Chaos and Nonlinear Dynamics: An Introduction for Scientists and Engineers* (Oxford University Press, Oxford, 2000).

[33] D. Gomila, M. A. Matías, and P. Colet, Phys. Rev. Lett. **94**, 063905 (2005); D. Gomila, A. Jacobo, M. A. Matías, and P. Colet, Phys. Rev. E **75**, 026217 (2007).

[34] C. Grebogi, E. Ott, and J. A. Yorke, Phys. D (Amsterdam) **7**, 181 (1983).

[35] P. Parra-Rivas, D. Gomila, M. A. Matías, and P. Colet, Phys. Rev. Lett. **110**, 064103 (2013); P. Parra-Rivas, D. Gomila, M. A. Matías, P. Colet, and L. Gelens, Opt. Express **22**, 30943 (2014); Phys. Rev. E **93**, 012211 (2016).

[36] J. Burke and E. Knobloch, Phys. Rev. E **73**, 056211 (2006).

[37] M. Tlidi and L. Gelens, Opt. Lett. **35**, 306 (2010); M. Tlidi, P. Kockaert, and L. Gelens, Phys. Rev. A **84**, 013807 (2011).

[38] S. Coen, H. G. Randle, T. Sylvestre, and M. Erkintalo, Opt. Lett. **38**, 37 (2013); S. Coen and M. Erkintalo, *ibid.* **38**, 1790 (2013); Y. K. Chembo and C. R. Menyuk, Phys. Rev. A **87**, 053852 (2013).

[39] P. Del'Haye, A. Schliesser, O. Arcizet, T. Wilken, R. Holzwarth, and T. J. Kippenberg, Nature (London) **450**, 1214 (2007); S. Cundiff, J. Ye, and J. Hall, Sci. Am. **298**, 74 (2008); T. J. Kippenberg, R. Holzwarth, and S. A. Diddams, Science **332**, 555 (2011); Y. Okawachi, K. Saha, J. S. Levy, Y. H. Wen, M. Lipson, and A. L. Gaeta, Opt. Lett. **36**, 3398 (2011); F. Ferdous, H. Miao, D. E. Leaird, K. Srinivasan, J. Wang, L. Chen, L. T. Varghese, and A. M. Weiner, Nat. Photon. **5**, 770 (2011); T. Herr, K. Hartinger, J. Riemensberger, C. Y. Wang, E. Gavartin, R. Holzwarth, M. L. Gorodetsky, and T. J. Kippenberg, *ibid.* **6**, 480 (2012); S. B. Papp, K. Beha, P. Del'Haye, F. Quinlan, H. Lee, K. J. Vahala, and S. A. Diddams, Optica **1**, 10 (2014).